Effect of different source terms ~~and inflow direction~~ in atmospheric boundary ~~modelling~~ modeling over the complex terrain site of Perdigao

Kartik Venkatraman[1,2,*], Trond-Ola Hågbo[1,3,*], Sophia Buckingham[1], and Knut Erik Teigen Giljarhus[3]

[1]von Karman Institute for Fluid Dynamics, Waterloosesteenweg 72, B-1640 Sint-Genesius-Rode, Belgium
[2]Université de Sherbrooke, Canada
[3]University of Stavanger, Norway
[*]These authors contributed equally to this work.

Correspondence: kartik.venkatraman@vki.ac.be

Abstract. ~~The assessment of~~ Assessing wind conditions in complex terrain requires Computational Fluid Dynamics (CFD) simulations incorporating an accurate parameterization of forest canopy effects and Coriolis effects. This study investigates how incorporating source terms such as the presence of trees and the Coriolis force can improve flow predictions. Furthermore, the study examines the impact of using different sets of atmospheric boundary layer inflow profiles, including idealized profiles with a logarithmic velocity profile, and a set of fully developed profiles from a pressure-driven precursor simulation. A three-dimensional steady Reynolds-averaged Navier-Stokes (RANS) equations model is set up using OpenFOAM to simulate the flow over a complex terrain site comprising two parallel ridges near Perdigão, Portugal. A 7.5 km × 7.5 km terrain of the Perdigao site is constructed from elevation data centered around a 100 m met-mast located on the Southwest ridge. A 30-min averaged stationary period is simulated, which corresponds to near-neutral conditions at met-mast Tower 20 located at the Southwest ridge. The period corresponds to the wind ~~is~~ coming from Southwest at 231° at 100 m height above ground at Tower 20. Five ~~different~~ case setups are simulated using a combination of different source terms, turbulence models and inflow profiles. The prediction capability of these models is analyzed for different groups of towers on the Southwest ridge and, on the towers further downstream inside the valley, and on the Northeast ridge. ~~The inclusion of~~ Including a canopy model improves predictions close to the ground for most of the towers on the Southwest ridge and inside the valley. Large uncertainties are seen in field measurement data inside the valley, which is a re-circulation zone and large prediction errors are seen in the wind velocity, wind direction and turbulent kinetic profiles for most of the models. The predictions on the Northeast ridge is dependent on the extent of re-circulation predicted inside the valley. The ~~precursor inflow model provides the best match for the wind velocity at Tower 29 on the Northeast ridge, while the canopy model shows a large under prediction~~ inflow wind direction from the South-West direction plays an important role in the wind profile predictions.

1 Introduction

Lack of terrain availability in flat terrain pushes wind-farm developers to look for alternatives along complex terrain sites. Flat terrain availability is becoming scarce and 70% of the Earth's surface is in complex terrain, which presents a large potential

for wind energy harvesting. Winds in complex terrains are governed by the surface properties of the flow (land class/roughness length) and the local elevation such as hills, ridges and mountains (Emeis 2018). Local features such as ridges or canyons can also be advantageous for wind energy harvesting, due to the creation of local flow accelerations on top of ridges and flow channeling through valleys. However, the wind fields ~~are dependent~~ depend on either the local pressure or temperature gradient. Such flows are also dominated by strong thermal stratification effects and are influenced by the presence of forest canopies. Complex terrain sites remain very challenging areas to consider for wind farm siting and require extensive validation of modeling tools in representative environments. Wind farm modeling for complex terrains requires a more advanced approach than commonly used cost-effective linearized models such as WAsP (Jørgensen et al., 2005) which cannot handle complex phenomena (i.e. flow separation) to ensure reliable and accurate results. Computational fluid dynamics (CFD) tools are increasingly used to predict flows over complex terrain sites to account for such phenomena and provide more accurate wind resource predictions (Blocken, 2014). However, improving numerical modeling tools for complex terrains demands accounting for various microscale phenomena such as flow re-circulation and the forest canopy effect. Such microscale flow features ~~have a significant impact on~~ significantly impact the local wind resource assessment and wind turbine loading.

Inital studies in literature accounting for the effects of forest canopy were performed over forested flat terrains. Brower (2012) showed that the presence of a forest canopy increases the ~~modelling~~ modeling uncertainty by up to a factor of 5 irrespective of the chosen ~~modelling~~ modeling approach. Finnigan (2000) parameterized the effect of foliage and forest canopy by accounting for the drag force in the momentum equation. The effect of the canopy on turbulence was further taken into account by Sogachev and Panfyorov (2006) and Sogachev (2009) by adding additional source terms for turbulence kinetic energy and turbulence dissipation rate. Desmond et al. (2017) ~~modelled~~ modeled both forest canopy and buoyancy effects by ~~modelling~~ modeling them using source and sink terms and showed that ~~the~~ thermal stratification plays an important role in determining the flow over canopies. The canopy model is typically implemented by specifying the tree height and leaf area density (LAD), which represents the area of the leaf and branches of trees. These parameters are typically defined from field measurements or LiDAR point clouds generated from field measurement campaigns and aerial surveys (Queck et al., 2012).

Validation of numerical models for complex terrains requires field measurements. One of the earliest field campaigns was at Askervin hill (Salmon et al., 1988), ~~which is~~ a smooth isolated hill. Similarly, the Bolund hill campaign was another campaign over an isolated hill in Denmark as detailed by Bechmann et al. (2009), with data under conditions ~~which~~ that could be classified as neutral. However, no canopy is seen on these sites. The Alaiz field campaign was performed over a ~~large scale~~ large-scale homogeneous mountain valley topography in Spain with forested regions (Rodrigo et al., 2021). Chavez et al. (2014) showed that using a canopy model improved the accuracy of velocity and turbulence predictions for simulations over Alaiz.

More recently, a field experiment campaign has been carried out over the complex terrain site at Perdigão, Portugal ~~,~~ by (Fernando et al., 2018), which is a double ridge with a forested canopy experiencing different thermal stratification conditions. Significant field data is available for further studies, and these are elaborated in Section 2. Several numerical studies have been performed for validation with field data. Laginha Palma et al. (2020) studied the choice of using the appropriate grid size for numerical ~~modelling~~ modeling. Wagner et al. (2019) implemented a forest parameterization in the Weather Research and Forecasting model (WRF) with an average tree height of 30 m, resulting in an improvement in ~~prediction of near surface~~

the prediction of near-surface wind speeds. This ~~was chosen due to~~ tree height was chosen for practical reasons related to the model setup and is not representative of actual tree height. There is a gap in the existing literature on microscale simulations using a canopy model on a heterogeneous forested complex terrain with a rich dataset such as Perdigão.

1.1 Objectives and outline

This paper aims to evaluate the impact of different physical source terms and turbulence models when performing CFD simulations in complex terrain and compare simulation prediction with field measurement profiles at the different groups of towers located at the Perdigão test site. The influence of the following parameters are investigated: Canopy effects, Coriolis force, and the effect of using two different sets of inflow profiles. One idealized set with a log-law velocity profile, and one set of fully developed profiles based on a precursor simulation. Furthermore, the influence of wind direction on the prediction of wind profiles is studied for the different case setups.

An improved understanding of the importance of these phenomena will enable the development of more efficient and reliable tools to perform wind simulations in complex terrain. This paper is structured as follows: a detailed description of the methodology is provided in Section 2, covering the computational domain and meshing, the numerical settings, and different modeling capabilities that have been added as source terms to the conservation equations. The results are presented and discussed in Section 3, in terms of different groups of towers. Section 4 is dedicated to concluding remarks and future perspectives. Finally, additional details on the mesh independence study, inflow profiles and wind direction study is provided in the Appendix.

2 Perdigão Field measurement campaign

An intensive observation period was carried out from 1 May 2017 to 15 June 2017 at the double ridge site of Perdigão, Portugal, by a consortium of American & European universities (Fernando et al. 2018). The location of the different met masts of heights 60 m and 100 m used in this study is shown in Fig. 2, which could be grouped by their location on top of the Southwest ridge, inside the valley, or at top of the Northeast ridge. From the analysis of the wind rose, the predominant directions at Tower 20 and Tower 29 are perpendicular to the ridges, i.e Northeast and Southwest directions, as shown in Fig. 1, while at Tower 25, flow turning is seen and the dominant wind direction is from the South.

(a) Tower 20 (tse04).   (b) Tower 25 (tse09).   (c) Tower 29 (tse13).
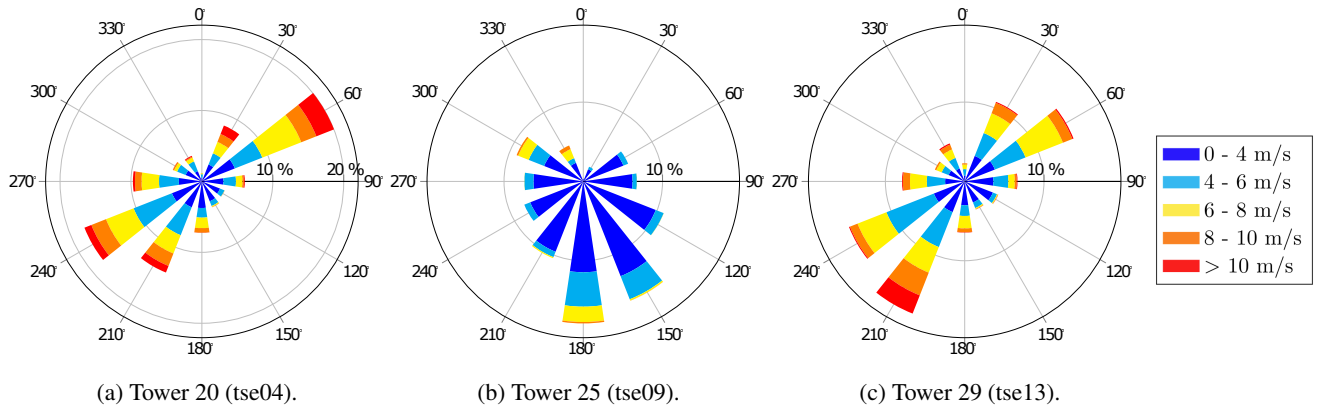
Figure 1. Wind rose for 1 month period of May 2017 for towers on top of the ridges and inside the valley.
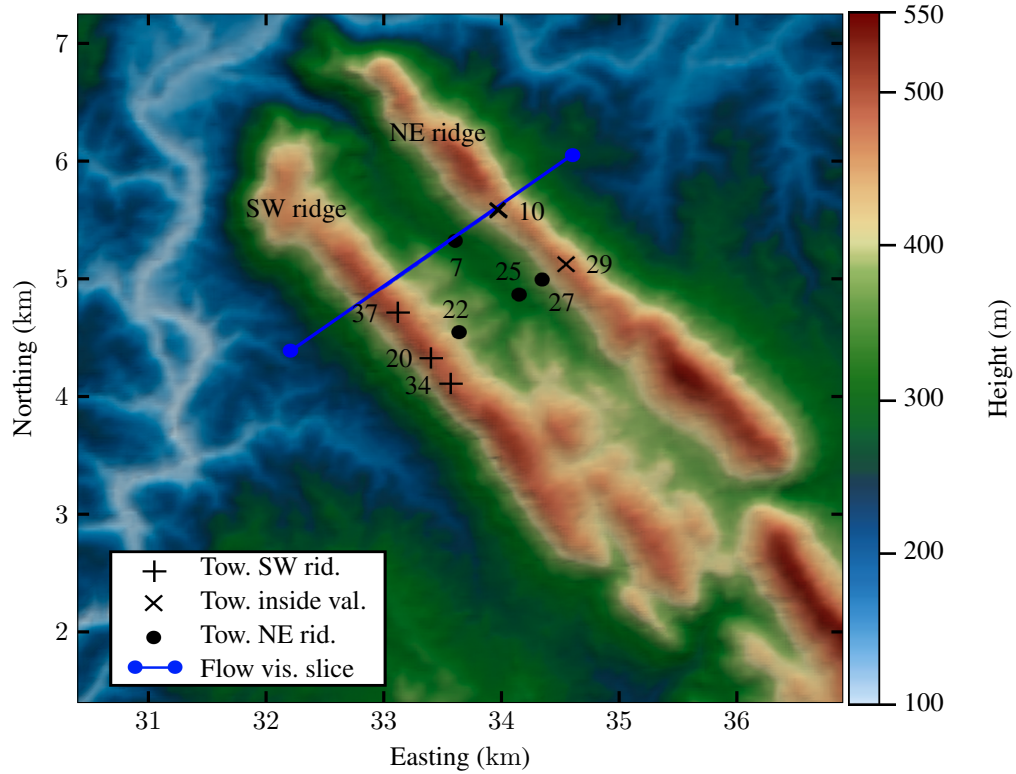
Figure 2. Elevation map and locations of interest at Perdigao. Positions of the measurements towers in the SW ridge group are indicated with + symbols, likewise are NE masts marked with x, and the masts in the inside valley group are indicated with black dots. The blue dots and the line represents the flow visualization slice used in Fig. 15. PT-TM06/ETRS89 coordinate system, height above sea level.

A stationary period was found on the date of 4th May, 2017 for the ~~30 minute~~ 30-minute averaged time interval of $22:00 - 22:30$ tilt corrected ~~high frequency~~ high-frequency dataset from NCAR-EOL, based on the conditions at Tower 20 on

top of the ridge, which corresponded to a Bulk Richardson number of approximately -0.03 which qualifies as near-neutral condition. The Bulk Richardson number as defined by Kaimal and Finnigan (1994) is calculated using Eqn. 1. However, the flow conditions are non-neutral at other met mast locations.

$$Ri_b = \frac{g(\bar{\theta_{100}} - \bar{\theta_2})\Delta z}{\bar{\theta_{100}}[U_{100}^2 + V_{100}^2]} \tag{1}$$

where θ is the potential temperature, g is the acceleration due to gravity, U, V are the wind velocity components at the reference height ~~(m)~~. The same period was simulated by Laginha Palma et al. (2020) based on the stationary periods predicted by Carvalho (2019).

3 Methodology

The terrain is a $7.5\,\mathrm{km} \times 7.5\,\mathrm{km}$ square centralized around a $100\,\mathrm{m}$ met-mast located on the Southwest ridge. Fig. 3 presents the computational domain and the dimensions are listed on the right side of the figure.

$H = 10 \times \Delta h_t = 4.4\,\mathrm{km}$
$R = 11.9\,\mathrm{km}$
$d_1 = 3.8\,\mathrm{km}$
$d_2 = 15 \times \Delta h_t = 6.6\,\mathrm{km}$
$\Delta h_t = 440\,\mathrm{m}$
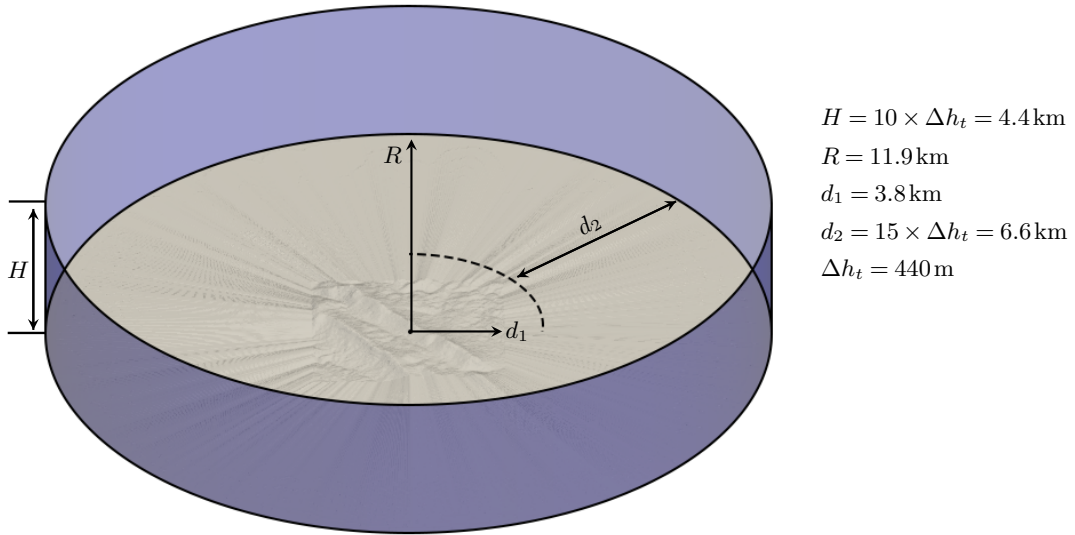
Figure 3. Computational domain, Δh_t is the difference in the elevation height of the terrain.

A cylindrical computation domain was developed, which provides the flexibility to simulate wind from any wind direction. ~~This approach has also been successfully applied by the authors in a previous study~~ The authors have successfully applied this approach in previous studies pertaining to urban areas (Hågbo et al. 2020) ( ). A smoothing region from complex to flat terrain was applied towards the outer boundaries, with a minimum radial distance of $15\,\Delta h_t$. Several best practice guidelines have been formulated for grid generation for simulating complex terrain sites, such as by Sørensen et al. (2012) and Laginha Palma et al. (2020) and have been closely followed. The height of the domain is set to ten times the difference in the elevation

height of the terrain, Δh_t, as recommended by Sørensen et al. (2012) when simulating wind flow over complex terrain sites. It consists of ~~12.7~~ approximately 88 million cells and is produced with `terrainBlockMesher` developed by (Schmidt et al., 2012), capable of generating structured meshes over complex terrain exclusively consisting of hexahedra cells. The `terrainBlockMesher` tool uses a blending function to smooth the transition from the terrain patch to the outer cylindrical block. Around 50 radial block cells are defined and a radial grading factor is used to enable a stretching in the horizontal direction to cluster cells across the ~~centre~~ center of the domain and ~~expanding~~ expand towards the boundaries. In terms of the number of cells per main direction ($N_x \times N_y \times N_z$) the mesh comprises of ~~227 x 227 x 120~~ 600 x 600 x 170 across the terrain patch. The vertical mesh resolution is ~~33 m~~ 24.5 m with uniform stretching applied across the entire domain. The minimal mesh height Δz next to the ground is close to 3 m. The average value of the wall y^+ is around 32,000. The mesh also follows the recommendation for having at least three cells from the ground to the height at the first sampling point for comparison with field measurements. The horizontal mesh resolution over the terrain was set close to $12.5\,\mathrm{m}$. It satisfies the minimum resolution of $40\,\mathrm{m}$ recommended specifically for the Perdigão site by Laginha Palma et al.~~(~~ (2020). Fig. 4 illustrates the grid structure used inside the domain from the side. Terrestrial data was obtained from the Shuttle Radar Topography Mission (SRTM) database of the Perdigão field experiment (Fernando et al. 2018). A mesh sensitivity study was performed and ~~is presented in the~~ presented in Appendix . The ~~grid resolution is sufficiently high and for the predictions in the area of interest close to the ridges where no significant changes were observed. However, increasing the refinement close to the ground has an impact on the predictions at met-mast locations close to the ground~~ results obtained with 3 different meshes of increasing resolution show negligible sensitivity on the wind profiles at three different towers on the ridges and inside the valley.

All simulations have been conducted using the OpenFOAM (version 2012) toolbox. The simulations are steady-state and performed by solving the incompressible, three-dimensional steady Reynolds-averaged Navier-Stokes (RANS) equations with the finite volume method. Second-order discretization schemes were used for ~~the~~ spatial discretization. The initial iterative convergence criteria were that the scaled residuals should drop four orders of magnitude for all flow variables as per the BPGs. Two steady-state solvers for turbulent flow of incompressible fluids have been used: `simpleFoam` (SF) and `buoyantBoussinesqSimpleFoam` (BBSF). All thermal effects are neglected in the simulations using both the solvers, such that the atmospheric stability of the simulated atmosphere is always neutral. In these simulations, the air density is assumed constant, and the gravitational force is neglected. The BBSF solver is capable of simulating the effect of buoyancy forces, but these source terms are set to zero for the present neutral case. However, in addition to solving the continuity equation and the momentum equation, which is solved using SF, the energy equation is also included, ~~which allows~~ allowing for the modeling of non-neutral atmospheric conditions.

3.1 Inlet profiles and boundary conditions

Two sets of fixed inlet profiles have been used, both forming a homogeneous atmospheric boundary layer (ABL), either idealized with a logarithmic velocity profile or fully developed profiles obtained from a precursor simulation.

The idealized profiles provide the turbulence quantities and a log-law type ground-normal wind velocity based on the generalization and modification of the well-used set of equations from Richards and Hoaxey (1993). This modification has been
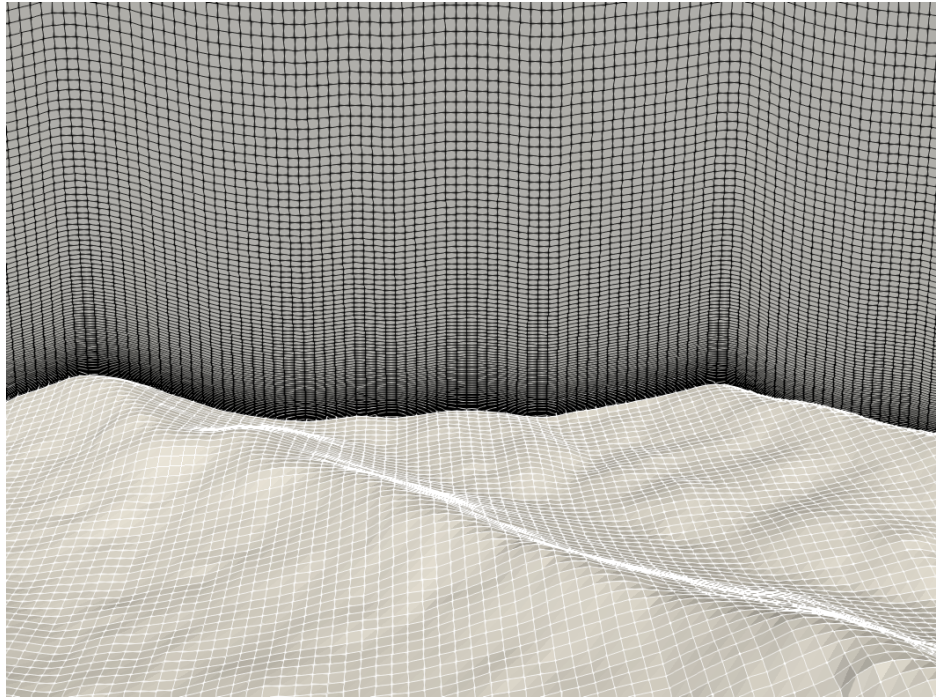
Figure 4. Computational grid structure, partial view from the side. The mesh used in this study consists of about 88 million cells, while the mesh presented in this figure is far coarser (about 10 million) for illustration purposes.

implemented by Yang et al. (2009) and uses a more mathematically consistent formulation allowing the turbulent kinetic energy to vary with height. Also, using a log-law wind velocity profile and the associated turbulent inflow conditions are considered

135   only to be valid in the atmospheric surface layer, which can be roughly estimated as 10% of the atmospheric boundary layer (Temel et al. 2018). The idealized velocity profile has no wind veer, meaning it does not have a changing wind direction with height.

An alternative to using the idealized profiles is using fully developed profiles obtained from a one-dimensional precursor simulation following the strategies of Koblitz (2013), Alletto et al.(2018). Cyclic conditions are applied on the sides, and

140   the simulations are run for sufficient iterations to allow the development of the profile. The setups are identical to the setups used in the final (successor) simulations except for the computational domain and mesh, the cyclic conditions applied, and the number of iterations. It enables the precursor simulations to produce inlet profiles valid for various conditions, including non-neutral atmospheric conditions. Adjusting the parameters of these source terms is an efficient way to obtain the desired inflow. The developed velocity profile has wind veer, meaning the wind turns clockwise with height caused by the balance

145   between friction, the Coriolis force, and the pressure gradient force, and that Perdigao is located in the Northern Hemisphere. : Also, the roughness length, z_0, was adjusted in the precursor simulations to obtain the right turbulent kinetic energy, TKE, at reference height. The inflow profiles are added in Appendix .

An overview of the boundary conditions (BCs) used is presented in Table 1.

Table 1. Overview of boundary conditions applied in the neutral simulation setup.

Patch	Boundary condition type
Sides	Inlet/outlet
Inlet	Fixed value profiles of an atmospheric boundary layer
Outlet	Zero gradient, and fixed pressure or fixed $(p - (\rho gh))$
Terrain	Rough wall, $z_0 = 0.02\,\mathrm{m}$
Top	Slip

Robin boundary conditions that act as an inlet or outlet are used on the sides of the domain to simulate wind from any
150 horizontal direction. The direction of the flux automatically determines the inlet and outlet regions. The inlet profiles are
fixed to form a homogeneous atmospheric boundary layer (ABL), either idealized profiles representing neutral atmospheric
conditions or fully developed profiles obtained from precursor simulation based on the work of (van der Laan et al., 2020).
Outlet conditions were used with constant pressure in the simulations using the SF solver, or equally, constant $(p - (\rho gh))$ in the
simulations using the BBSF solver. Zero gradient was set for the remaining variables. The direction of the flux automatically
155 determines the inlet and outlet regions. No-slip conditions with wall functions were used for the terrain. Specifically, a rough
wall condition was applied (Hargreaves and Wright, 2007). The roughness length was set to $z_0 = 0.02\,\mathrm{m}$, based on average
values of a roughness ~~map provided at~~ length map provided in the database of the Perdigão field experiment (Fernando et al.,
2018).

3.2 Source terms

160 Three different source terms have been added to the momentum equation for some ~~of the~~ simulation cases: Tree canopy as a
porous medium, Coriolis force, and pressure gradient force. Additionally, a limiter in the turbulence dissipation equation was
added to one of the cases.

The canopy is modeled as a porous medium based on the work of Costa (2007). A drag term is added to the momentum
equation. The canopy source term was utilized with the `simpleFoam` (SF) flow solver. The porosity model is based on the
165 `powerLawLopesdaCosta` model implemented in OpenFOAM. It is a variant of the power law porosity model with a spa-
tially varying drag coefficient. This source term is applied to the momentum equation to reproduce the momentum dissipation
that the trees and ~~its~~ their foliage should produce in the flow. The following parameters are used: Porosity surface area per
unit volume or the leaf area density ($\Sigma = 1.0$), Drag coefficient ($C_d = 0.25$), and the Power law model exponent coefficient
($C1 = 2.0$) for the Equation 2. A mean tree height of $3\,\mathrm{m}$ is chosen based on the mean canopy height at different locations
170 provided by Vasiljevic et al. (2017). This was applied all over the entire flow domain. A cell set was ~~utilized~~ used to select
a volume of cells 3 m above the ground (~~this~~ which forms a canopy zone where the source terms are activated). An over-

all tree height of $3\,\mathrm{m}$ is also supported by analyzing a LiDAR point cloud acquired from the database of the Perdigão field experiment (Fernando et al., 2018) as shown in Fig. 5. The source term in the canopy model for velocity is as shown below:

$$S_p- = \alpha\rho\left(C_d\Sigma\left|u_o\right|\right)u \tag{2}$$

175   where Σ is the Leaf area density, C_d is the plant canopy drag coefficient. As highlighted in Lalic and Mihailovic (Lalic and Mihailovic, 2004), forests have a higher foliage density at the half top than at the bottom zones. However, for the present case, simulations are performed with a uniform leaf area density.
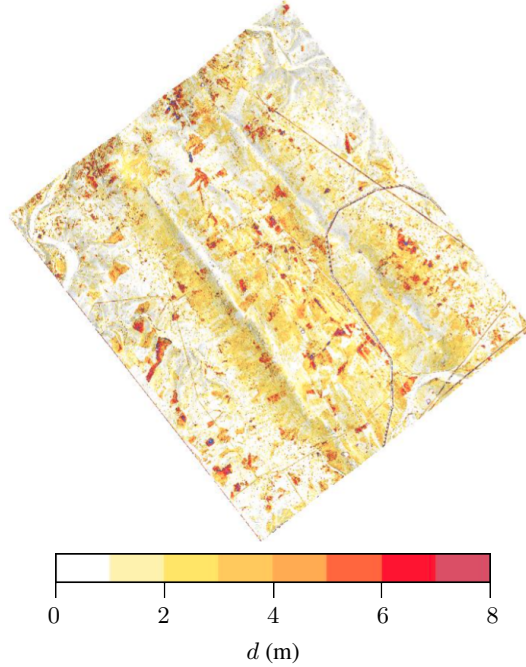
Figure 5. Minimum Euclidean distance, d, from the trees/vegetation to the bare ground effectively showing their height. Results obtained from analyzing a LiDAR point cloud acquired from the database of the Perdigao Field Experiment website *https://perdigao.fe.up.pt/*.

The Coriolis force source term is included as a momentum source term (U and V momentum equations). The Coriolis force is calculated based on the planetary rotational period ($\Omega = 24\ h$) and the latitude (λ) for Perdigao (39.68 °N), where

180   ~~$f_c = 2\Omega sin(\lambda)$~~$f_c = 2\Omega\sin(\lambda)$. Similar to Koblitz ~~2013~~(2013), the Coriolis force in the vertical direction is neglected since it is negligible compared to the gravitational acceleration.

A pressure gradient forcing term is also included in the simulation cases using the BBSF solver. In setups using this solver, the wind is driven by the balance of the lateral pressure gradient force and the Coriolis force, which are added in the momentum equation as shown in equations provided in the Appendix . This balance is called geostrophic balance, and the resulting wind

185   is a geostrophic wind, which in the Northern Hemisphere goes counterclockwise around low-pressure systems.

The level of turbulent kinetic energy is controlled in the domain by the use of a parameter called the maximum turbulent mixing length scale, used ~~is~~ to limit the production and dissipation terms of the turbulence model. ~~The maximum global turbulent mixing length scale for a neutral ABL as is shown in Eq. ?? proposed by Blackadar (1962) and also used by Koblitz (2013).~~ Ambient source terms were added to avoid zero turbulence values above the ABL similar to those mentioned in (van der Laan et al., 2021a) and applied to the entire domain. The values were set to $k_{Amb} = 0.001$ and $\epsilon_{Amb} = 7.208e - 08$ as summarized in Table 3.

$$L_o = 0.00027 \frac{G}{f_c}$$

~~where G is the geostrophic wind and f_c is~~ The geostrophic wind is denoted by G and the Coriolis frequency parameter ~~.~~ is denoted by f_c. The governing equations for the BBSF solver and the different source terms are further detailed in ~~the~~ Appendix .

3.3 Simulation cases

The setup for all the simulations was identical except for certain parameters. The solver used is either `simpleFoam` (SF) or `buoyantBoussinesqSimpleFoam` (BBSF). The inlet profiles, either idealized with a logarithmic velocity profile representing neutral atmospheric conditions or fully developed profiles obtained from precursor simulation. Source terms added, including canopy (tree height set to $3\,\mathrm{m}$) and the Coriolis force. Three turbulence models have been used: the standard k-ϵ turbulence model (SKE), a modified k-ϵ turbulence model (MKE), and the k-ω turbulence model (KO). The MKE model is applied in the simulation case where trees/vegetation (canopy) has been added as a porous medium with the SF solver. The turbulent ~~constans~~ constants are modified with $C_\mu = 0.033$. This model was tuned using experimental data and LES (Large Eddy Simulation) for a homogeneous forest (Costa 2007). ~~With regards to the boundary conditions , they~~ The boundary conditions are overall the same but had to be adjusted to account for the different solvers and inlet profiles used. An overview of all the simulation cases is provided in Table 2. The set of chosen turbulence constants ~~are~~ is shown in Table 3.

Table 2. List of simulation cases simulating a period of neutral atmosphere, 22:00-22:30 (04.05.17).

Case name	Solver	Inlet profiles	Source terms			Turbulence mod.
			Canopy	Coriolis	Pres. gr.	
SF1	SF	Idealized	No	No	No	SKE
SF2	SF	Idealized	No	No	No	KO
SF3	SF	Idealized	Yes	No	No	MKE
SF4	SF	Idealized	No	Yes	No	SKE
BBSF1	BBSF	Precursor	No	Yes	Yes	KE-Lim

Numerical convergence difficulties can be encountered when using the global turbulence length scale limiter (van der Laan et al., 2021b) when applied to the present case for simulations over the complex terrain of Perdigao. ~~This is especially true~~ These convergence difficulties can be particularly challenging when setting the values of the maximum limiting length scale to low values. Here, the model is trying to restrict the turbulence scale, but physically the large length scales of turbulence are produced from hills or features that ~~are~~ are in the order of the maximum value that is set by turbulence model.

Table 3. Turbulence constants for different turbulence models.

Coefficient	Turbulence model			
	SKE	MKE	KO	KE-Lim
C_μ	0.09	0.033	0.09	0.09
C1	1.44	1.44	-	1.44
C2	1.92	1.92	-	1.92
σ_ϵ	1.30	1.85	-	1.30
σ_K	1.0	-	0.5	-
α_K	-		0.5	-
α_ω	-	-	0.6	-
$\beta*$	0.09	-	-	0.09
β	-	-	0.072	-
ν	1.5e-05	1.5e-05	1.5e-05	1.5e-05
L_{max}	-	-	-	62.14
k_{Amb}	-	-	-	0.001
ϵ_{Amb}	-	-	-	$7.208e-08$
T_{Ref}	-	-	-	300
Pr	-	-	-	0.9
Prt	-	-	-	0.74
G	-	-	-	6.2
f_c	-	-	-	0.929e-4

4   Results

The results are discussed based on three groups of towers of interest: on top of the Southwest ridge, inside the valley and on top of the Northeast ridge. The inlet profiles for all the simulations are calibrated to match the measured velocity magnitude and direction at 100 m at tower 20, which corresponds to an elevation of 573 m. Different metrics are analyzed for all the simulation models at different towers and are further explained. The root mean square error (RMSE) between the averaged profiles of the measured data and the simulated results is computed and presented in Table 4. A hit rate metric for a given model is defined as the number of predictions within one standard deviation over each height of the field measurement. The relative error for the

Table 4. RMSE for wind speed predictions on the main towers of interest.

Case	Weather mast and group	RMSE (m/s) Height over terrain							Average RMSE (m/s)	Hit rate (max 7)
		10 m	20 m	30 m	40 m	60 m	80 m	100 m		
SF1 (k-ϵ)	Tower 20 (SW rid.)	0.70	0.16	0.14	0.11	0.17	0.05	0.05	0.20	6
	Tower 25 (valley)	1.40	1.3	1.21	1.01	0.73	0.49	0.27	0.92	6
	Tower 29 (NE rid.)	1.81	1.18	1.01	0.67	0.43	0.58	0.71	0.91	3
SF2 (k-ω)	Tower 20 (SW rid.)	0.73	0.21	0.19	0.16	0.18	0.04	0.05	0.22	6
	Tower 25 (valley)	1.89	1.91	1.93	1.9	1.83	1.68	1.51	1.81	0
	Tower 29 (NE rid.)	1.59	0.86	0.71	0.43	0.22	0.43	0.61	0.69	6
SF3 (canopy)	Tower 20 (SW rid.)	0.65	0.53	0.46	0.38	0.37	0.19	0.06	0.38	2
	Tower 25 (valley)	0.37	0.42	0.36	0.21	0.1	0.37	0.57	0.34	1
	Tower 29 (NE rid.)	2.03	2.56	2.77	2.7	2.75	2.73	2.71	2.61	0
SF4 (Coriolis)	Tower 20 (SW rid.)	0.75	0.31	0.28	0.24	0.29	0.15	0.14	0.31	6
	Tower 25 (valley)	0.88	1.24	1.3	1.22	1.25	1.21	1.29	1.20	5
	Tower 29 (NE rid.)	1.47	0.59	0.29	0.09	0.47	0.29	0.24	0.49	6
BBSF1 (k-ϵ Lim)	Tower 20 (SW rid.)	1.33	0.73	0.71	0.66	0.37	0.41	0.35	0.65	4
	Tower 25 (valley)	1.15	1.46	1.53	1.51	1.61	1.64	1.7	1.51	3
	Tower 29 (NE rid.)	1.41	0.66	0.5	0.24	0.2	0.35	0.56	0.56	6

220 turbulent kinetic energy and wind direction is shown in Tables 5, 6 respectively. The relative error is ~~defined as the percentage of~~ given in percentage and is the difference between the simulated and field measurement ~~, which is divided by~~ divided by the field measurement value. The error bars represent the standard deviation of the mean measurements.

4.1 Model prediction on SW ridge

The towers on the SW ridge as shown in Fig. 2, are the Tower 20, 34 and 37. This is a region of flow acceleration. The inflow
225 profile is calibrated to match the velocity at 100 m height for Tower 20 as shown in the wind velocity profiles shown in Fig. 6 (a) at 100 m. All models except the canopy model (SF3) ~~shows~~ show an over prediction of the velocity profiles close to the ground at Tower 20. The canopy model (SF3) underpredicts the velocity close to the ground but ~~correctly predicts the decrease in velocity close to the ground~~accurately captures the shape of the profile. This prediction could be improved by considering a ~~non uniform~~ non-uniform tree height and removing the canopy source terms on top of the ridges. On the other hand, at Tower
230 34, shown in Fig 6 (b), the canopy model (SF3) shows a good match with the field measurement, and on Tower 37 seen in Fig 6 (c), shows a slight under prediction. In models that do not account for a canopy (SF1, SF2, SF4 and BBSF1), a speed-up is seen close to the ground with large RMSE errors as shown in Table 4. The results suggest that the inclusion of the canopy is a good choice for ~~prediction~~ predicting of velocity profiles~~, however~~. However, the canopy parameters need to be adapted based on the forest point cloud data. BBSF1 model (k-ϵ Lim) shows a higher speed-up close to the ground at most of the towers. The

Table 5. Relative error and hit rate metrics for turbulent kinetic energy predictions at the main towers of interest.

Case	Weather mast and group	Average relative difference in TKE (%)	Hit rate (max 7)
SF1 (k-ϵ)	Tower 20 (SW rid.)	11.61	7
	Tower 25 (valley)	51.24	7
	Tower 29 (NE rid.)	35.53	4
SF2 (k-ω)	Tower 20 (SW rid.)	10.36	7
	Tower 25 (valley)	23.08	7
	Tower 29 (NE rid.)	33.69	7
SF3 (canopy)	Tower 20 (SW rid.)	96.98	0
	Tower 25 (valley)	46.2	7
	Tower 29 (NE rid.)	25.49	7
SF4 (Coriolis)	Tower 20 (SW rid.)	12.61	7
	Tower 25 (valley)	49.91	7
	Tower 29 (NE rid.)	55.51	2
BBSF1 (k-ϵ Lim)	Tower 20 (SW rid.)	10.21	7
	Tower 25 (valley)	51.57	7
	Tower 29 (NE rid.)	55.44	1

Table 6. Relative error and hit rate metrics for wind direction predictions at the main towers of interest.

Case	Weather mast and group	Average difference in wind direction (°)	Hit rate (max 7)
SF1 (k-ϵ)	Tower 20 (SW rid.)	1.14	6
	Tower 25 (valley)	14.02	7
	Tower 29 (NE rid.)	8.42	4
SF2 (k-ω)	Tower 20 (SW rid.)	1.18	6
	Tower 25 (valley)	18.39	7
	Tower 29 (NE rid.)	6.45	5
SF3 (canopy)	Tower 20 (SW rid.)	1.3	7
	Tower 25 (valley)	10.93	7
	Tower 29 (NE rid.)	10.25	3
SF4 (Coriolis)	Tower 20 (SW rid.)	1.79	6
	Tower 25 (valley)	49.41	2
	Tower 29 (NE rid.)	3.18	7
BBSF1 (k-ϵ Lim)	Tower 20 (SW rid.)	5.63	1
	Tower 25 (valley)	41.8	3
	Tower 29 (NE rid.)	4.39	7

235 turbulent kinetic energy profiles are shown in Fig 7, showing a good prediction for all the models except the Canopy model (S3) which produces excessive turbulence levels compared to field measurements. ~~BBSF1 model (k-ε Lim) shows a good match to the field measurement at Towers 20 and 34.~~ Fig 8 shows the predicted wind direction profiles at the three towers ~~. The BBSF1 model (k-ε Lim) shows the best prediction for the wind direction overall as seen in Table 6~~showing a good prediction for most of the models within one standard deviation of the measurements. As highlighted in the methodology section, there is a large

240 uncertainty in wind direction seen in the field experiment that varies with location and height ~~, and for a complex terrain a small change inflow direction could play an important role in the predicted wind direction profiles at the mast. This~~ which is further investigated in Section 4.4 for two additional wind directions. This uncertainity highlights a limitation in the models' ability to represent actual conditions for such a complex site. ~~SF4 model (Coriolis) shows a large wind veer that affects the wind direction prediction, which indicates that this needs to be tuned in the inflow profile for this model to account for this~~

245 ~~flow turning.~~ In terms of the turbulence model, the SF1 model (k-ε) is seen to produce a slightly greater ~~speed up~~ speed-up compared to the SF2 model (k-ω)~~, but~~ . Still, overall the prediction capability for the wind speed, turbulent kinetic energy, and wind speed is similar.
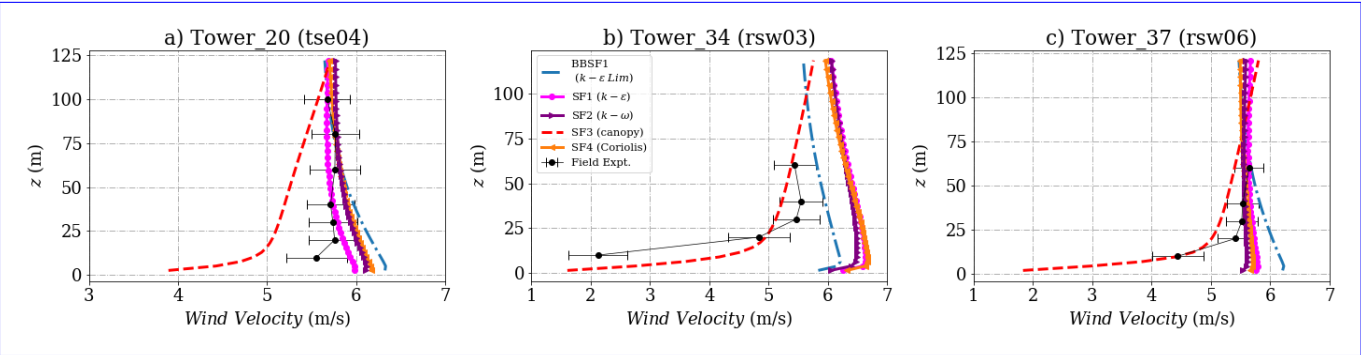
Figure 6. Simulation results and experimental data for wind velocity on the Southwest ridge for a) Tower 20 (tse04) b) Tower 34 (rsw03) c) Tower 37 (rsw06). The locations of the masts are given in Fig 2.

4.2 Model prediction inside the valley

The towers of interest inside the valley are Towers 25, 7, 27 and 22 as seen earlier in Fig 2. The valley is a region of strong

250 flow separation and flow re-circulation. The predicted velocity profiles are shown in Figs. 9 and 10 with different predictions of the extent of re-circulation zones, resulting in various shapes of the wind profiles. At Towers 25, 22 and 27 the canopy model significantly underpredicts the velocity profiles. ~~On the other hand, the canopy model shows the~~ The SF2 (Canopy), SF1 (k − ε) and SF2 (k − ω) show the best prediction at Tower 7, which is located ~~the lowest in~~ at the lowest altitude among the other towers. ~~The BBSF1 model overestimates the velocity at Tower 25 and all models show an under prediction at Tower 22.~~

255 ~~The~~ Overall the SF1 ~~(k − ε)~~ model ~~performs better than the SF2 (k − ω) model in prediction of wind velocity~~shows the best prediction at all the towers inside the valley.
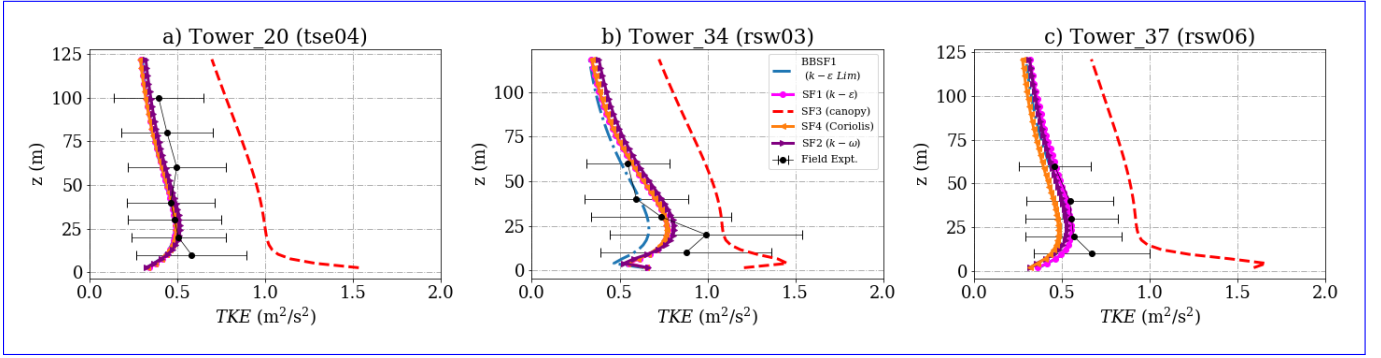
Figure 7. Simulation results and experimental data for turbulent kinetic energy on the Southwest ridge for a) Tower 20 (tse04) b) Tower 34 (rsw03) c) Tower 37 (rsw06). The locations of the masts are given in Fig 2.
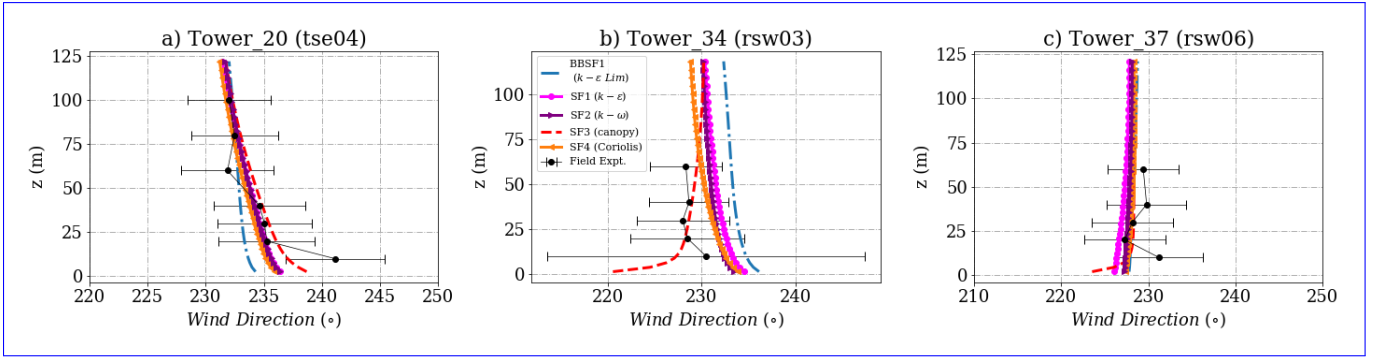
Figure 8. Simulation results and experimental data for wind direction on the Southwest ridge for a) Tower 20 (tse04) b) Tower 34 (rsw03) c) Tower 37 (rsw06). The locations of the masts are given in Fig 2.
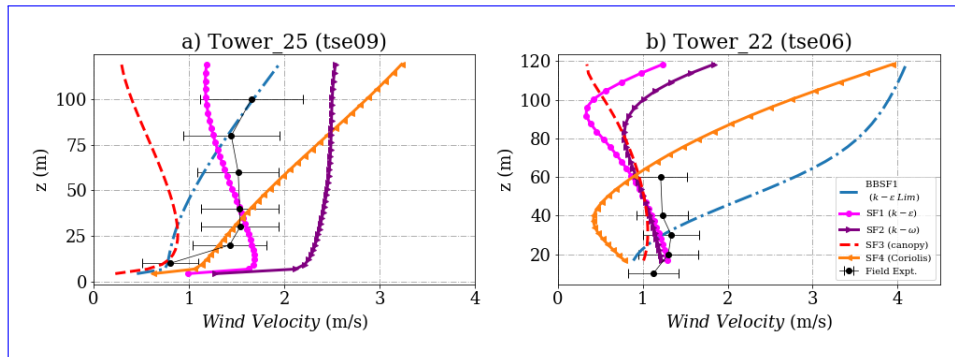
Figure 9. Simulation results and experimental data wind velocity inside the valley for a) Tower 25 (tse09) b) Tower 22 (tse06). The locations of the masts are given in Fig. 2.
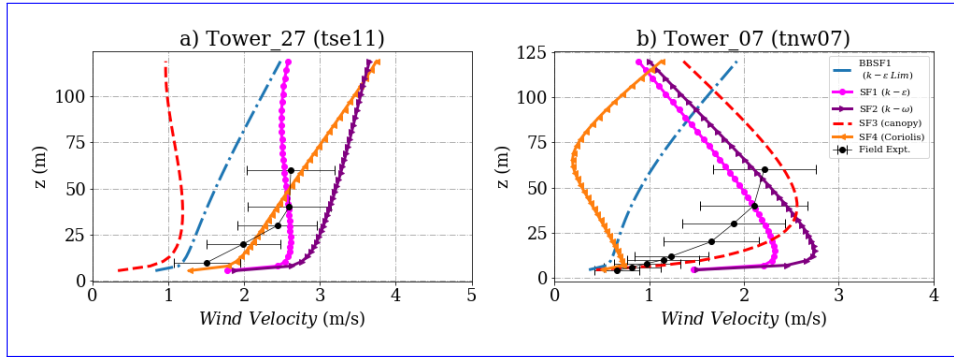
Figure 10. Simulation results and experimental data for wind velocity inside the valley for a) Tower 27 (tse11) b) Tower 7 (tnw07). The locations of the masts are given in Fig. 2.

Figs. 11 and 12 show a comparison of turbulent kinetic energy profiles between the present model predictions and the field measurements. The measured values of turbulent kinetic energy are high inside the valley at all met-mast locations, indicative of flow mixing and high turbulence, ~~however~~. However, all the models seem to strongly underpredict the turbulent kinetic energy with large relative errors as seen in Table 5, except for Tower 22, which is located the closest to the Southwest ridge.
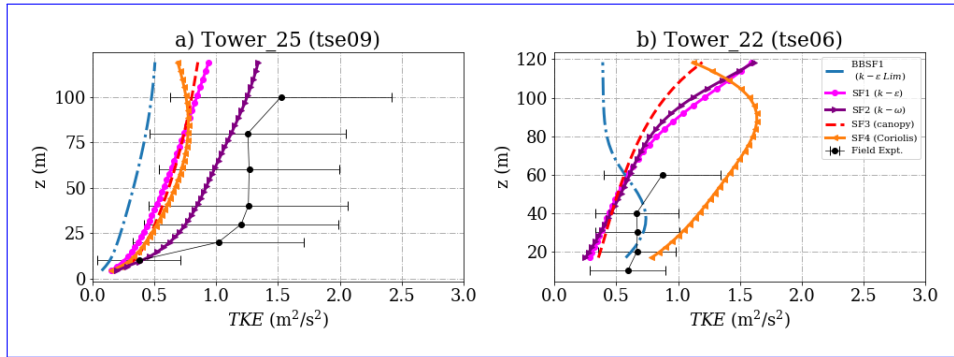
Figure 11. Simulation results and experimental data for turbulent kinetic energy inside the valley for a) Tower 25 (tse09) b) Tower 22 (tse06). The locations of the masts are given in Fig. 2.

The wind direction profiles are shown in Figs. 13 and 14 respectively. A sudden shift in wind direction, indicative of ~~a~~ flow separation and re-circulation is seen in Fig. 13. ~~The BBSF1 model (k-ε Lim) provides a good~~ Table 6 provides the hit rate for ~~the wind direction inside the valley as shown in Table 6~~ different models at all the towers. Fig. 15 shows the velocity contour for the predicted re-circulation zone inside the valley for the SF3 model (canopy) and the BBSF1 model (k-ε Lim). The SF3 model (canopy) produces a single large re-circulation zone compared to the other models, and a smaller and double re-circulation zone is seen for the BBSF1 model (k-ε Lim). ~~This is seen as a large~~ The large recirculation zone results in a significant under prediction of the velocity profiles seen earlier in Figs. 9 and 10 for the canopy model.
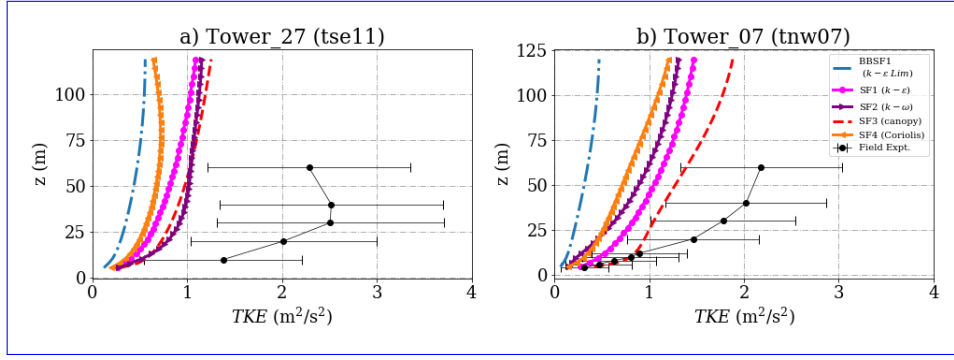
Figure 12. Simulation results and experimental data for turbulent kinetic energy inside the valley for a) Tower 27 (tse11) b) Tower 7 (tnw07). The locations of the masts are given in Fig. 2.
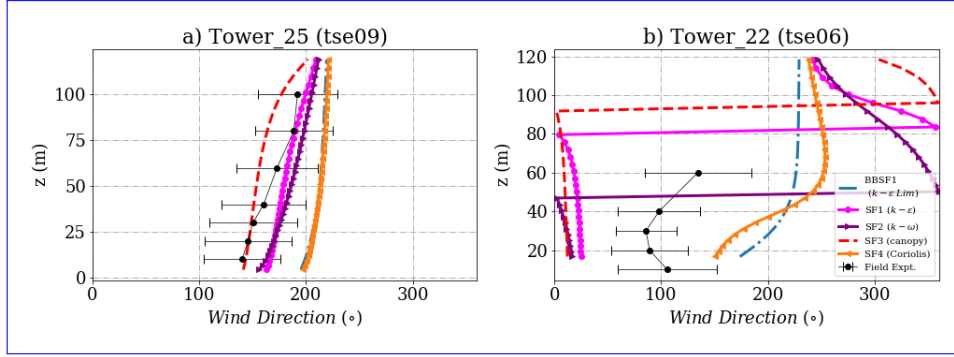
Figure 13. Simulation results and experimental data for wind direction inside the valley for a) Tower 25 (tse09) b) Tower 22 (tse06). The locations of the masts are given in Fig. 2.
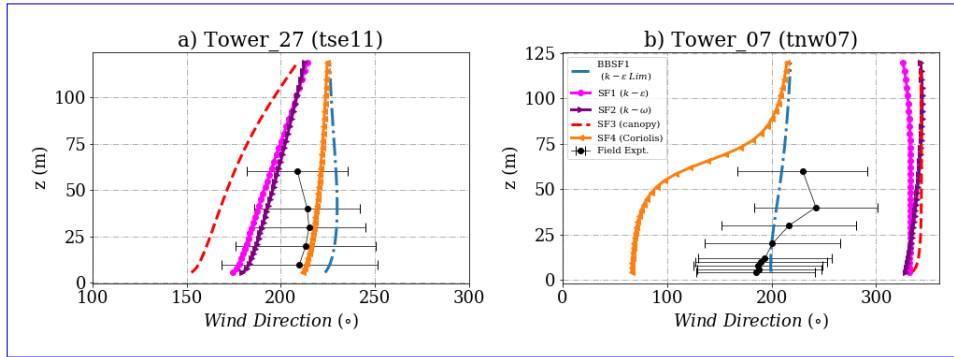
Figure 14. Simulation results and experimental data for wind direction inside the valley for a) Tower 27 (tse11) b) Tower 7 (tnw07). The locations of the masts are given in Fig. 2.
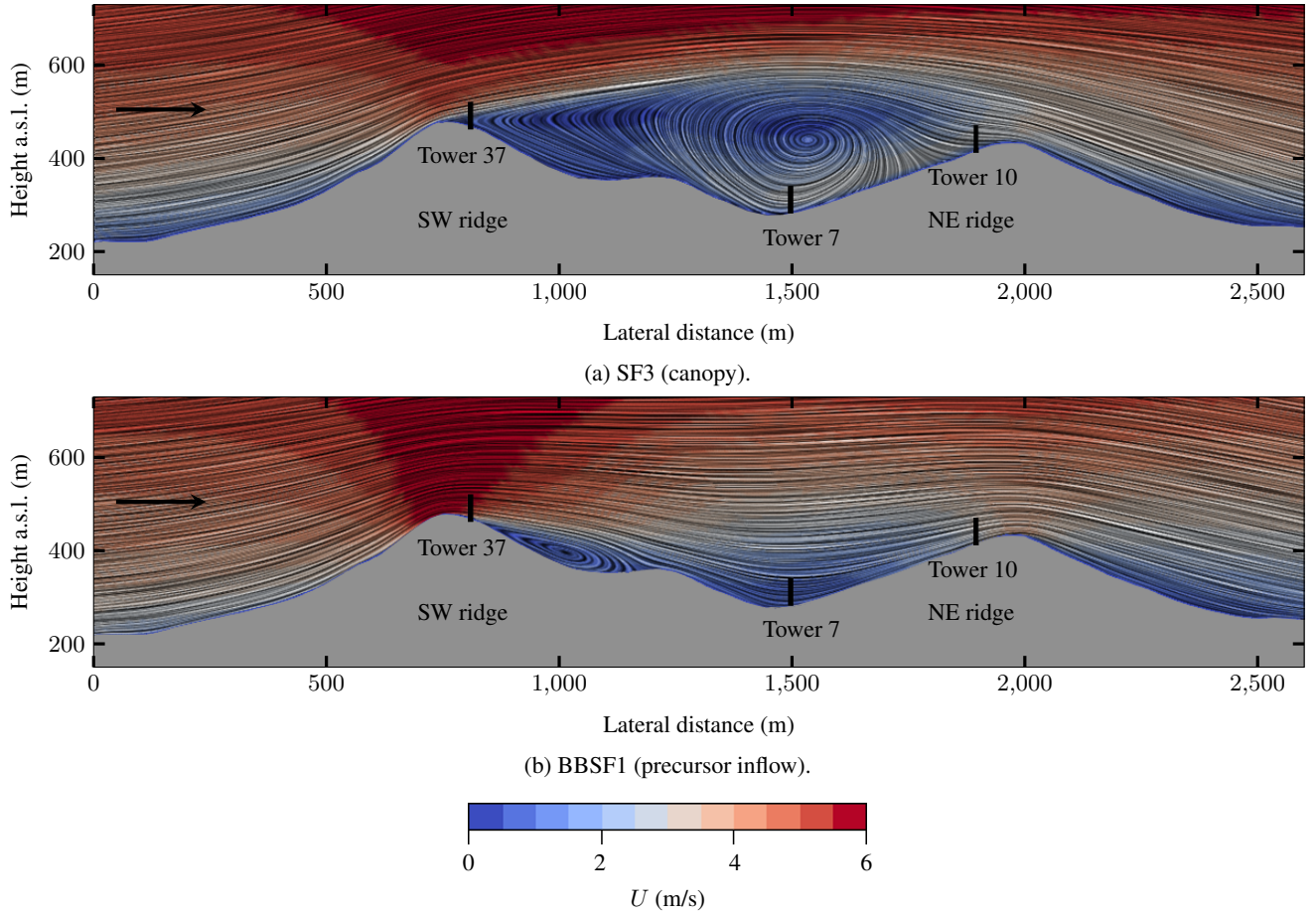
Figure 15. Vertical slice illustrating the re-circulation zones inside the valley. Flow patterns and velocity magnitude, U, are visualized through the technique line integral convolution (LIC). The black lines represent the location and height of the nearest measurement towers in front of or behind the slice. The black arrows indicate the wind direction at the inlet, wind from SW at $231°$, which is parallel to the orientation of the presented slice. The slice location and the locations of the masts are given in Fig. 2.

4.3 ~~Tower~~ Model Prediction on NE ridge

The wind velocity profiles for Tower 29 and Tower 10 on the Northeast ridge are shown in Fig. 16. This area on the top of a
270   ridge is a region of flow acceleration~~on top of the ridge downstream from~~. It is just downstream from the re-circulation zone
inside the valley, which makes the predictions quite challenging. The SF3 model (canopy) is seen to under predict ~~significantly~~
the velocity profiles significantly on top of this ridge. ~~Both the baseline SF1 ($k - \epsilon$) model and the BBSF1 model (k-ϵ Lim)~~
~~appears~~ All other models appear to provide a good prediction of the velocity profile ~~and wind direction for the Tower 29.~~
around one standard deviation of the field measurements. The region near Tower 10 comprises ~~of~~ a mountain gap (Vassallo
275   et al. 2020), ~~which could indicate that a higher terrain resolution is required surrounding this region to improve the prediction~~
~~accuracy. Excessive levels of turbulence is~~ where the local flow features could play an important role. The SF3 (Coriolis) and
the BBSF1 models predict the profiles close to the field measurement. Excessive turbulence levels are seen close to the ground
in the field measurements shown in Fig. 17. All models appear to underpredict the field measurements of turbulence close to
the ground, and the SF3 (canopy) shows the closest match. The BBSF1 model (k-ϵ Lim) underpredicts the turbulence levels
280   , due to the use of the maximum length scale limiter. The wind direction profiles at the towers are shown in Fig. 18. As seen
for the TKE profiles, a large uncertainty is seen in the wind direction on this ridge, this is expected as the wind is from the
Southwest direction. Most of the model predictions fall within one standard deviation of the measurements at Tower ~~29 except~~
~~for the SF4 (Coriolis) model.~~ 29. As seen in Fig. 15, the prediction of wind direction at Tower 10 is dependent on the extent of
re-circulation zone and flow reattachment location on top of the ridge.
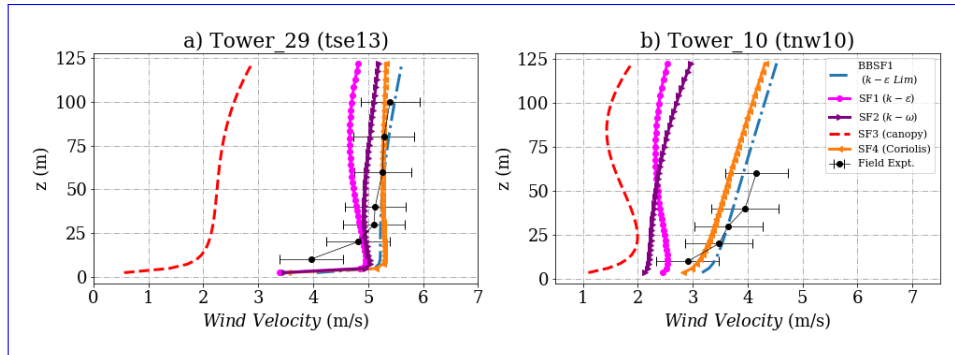
Figure 16. Simulation results and experimental data for wind velocity on the Northeast ridge for a) Tower 29 (tse13) b) Tower 10 (tnw10).
The locations of the masts are given in Fig. 2.

285   4.4 Influence of wind direction

The inflow direction plays an essential role in the wind predictions for complex terrains. A wind direction standard deviation
of around $7°$ is seen in the field measurements at Tower 20 (tse04). Simulations have been performed for two additional wind
directions $(231 \pm 3.5°)$ for each model to look at the differences observed between the three incoming wind directions.
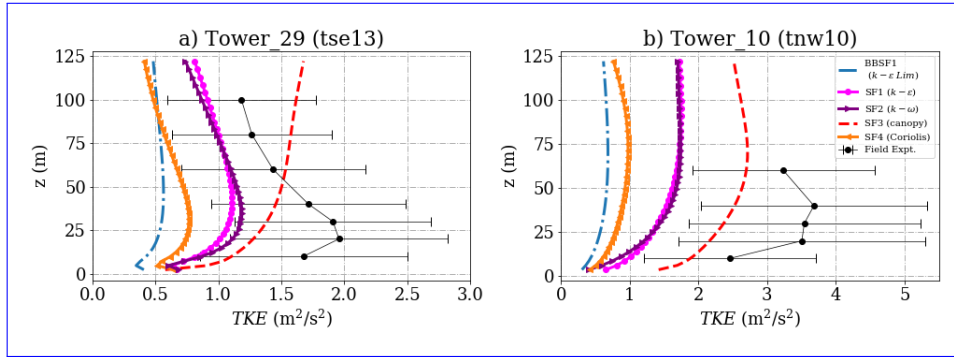
Figure 17. Simulation results and experimental data for turbulent kinetic energy on the Northeast ridge for a) Tower 29 (tse13) b) Tower 10 (tnw10). The locations of the masts are given in Fig. 2.
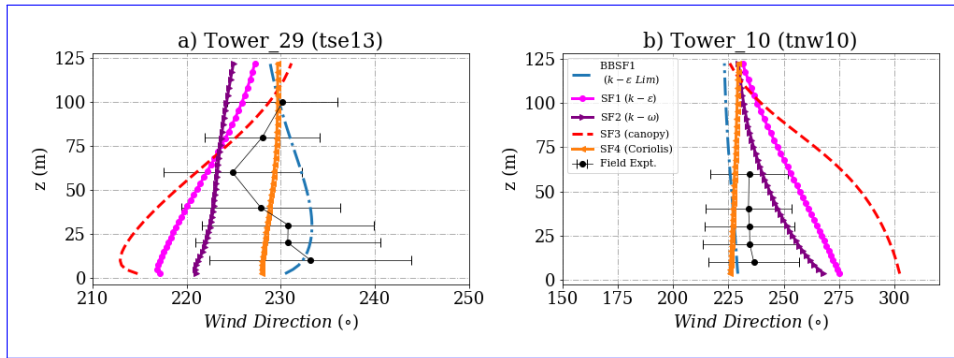
Figure 18. Simulation results and experimental data for wind direction on the Northeast ridge for a) Tower 29 (tse13) b) Tower 10 (tnw10). The locations of the masts are given in Fig. 2.

The results for the model predictions using the SF1 ($k - \epsilon$) model are presented in this section, while the results obtained using the other models of this study are shown in Appendix. For each model, the wind profiles at three different met-masts, corresponding to Tower 20 (tse04) on the South-West ridge, Tower 25 (tse09) inside the valley, and Tower 29 (tse13) on the North-East ridge are shown.

All simulations are calibrated for Tower 20 as seen in Fig 19 with the same inflow velocity at the reference height of 100 m on the tower and only changing the wind direction. The predicted profiles inside the valley and on the North-East ridge appear to vary quite significantly with the inflow wind direction as seen in Figs 20 and 21. Streamline trajectories for the inflow with three different wind directions at the Towers are shown in Fig 22. Wind passing through Tower 29 with inlet wind from 234.5° exhibits a very different trajectory compared to the other inlet wind directions and the set of trajectories passing through the mast upstream, Tower 20. The wind here was initially deflected off from the NE ridge and led into the valley by a channelling effect. As a result, the wind speed decreases significantly before passing Tower 29, before re-gaining in intensity downstream of the ridge as the wind accelerates downhill.
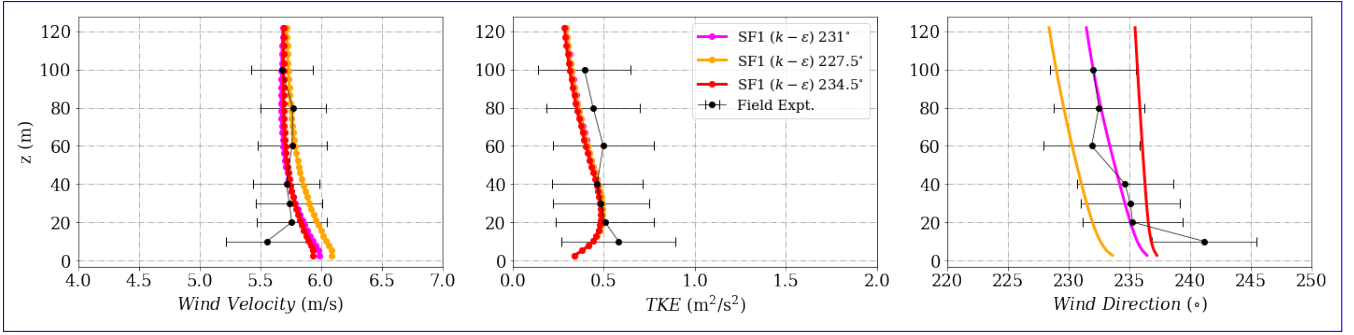
Figure 19. Simulation results and experimental data for wind velocity on the Southwest ridge for a) Tower 20 (tse04). The locations of the masts are given in Fig 2.
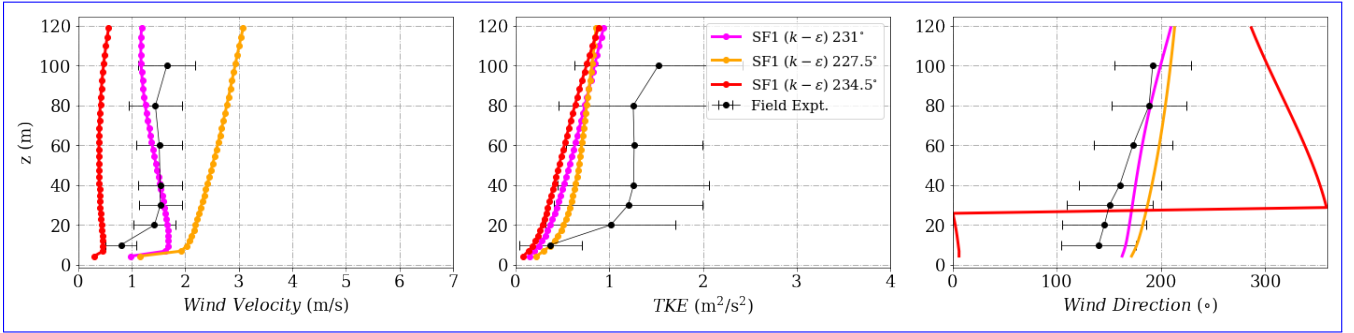
Figure 20. Simulation results and experimental data wind velocity inside the valley Tower 25 (tse09).
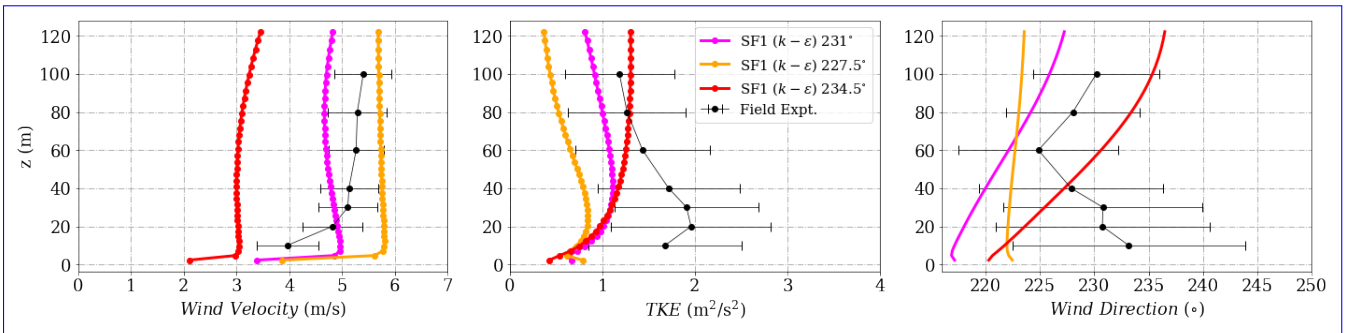
Figure 21. Simulation results and experimental data for wind velocity on the Northeast ridge for Tower 29 (tse13).
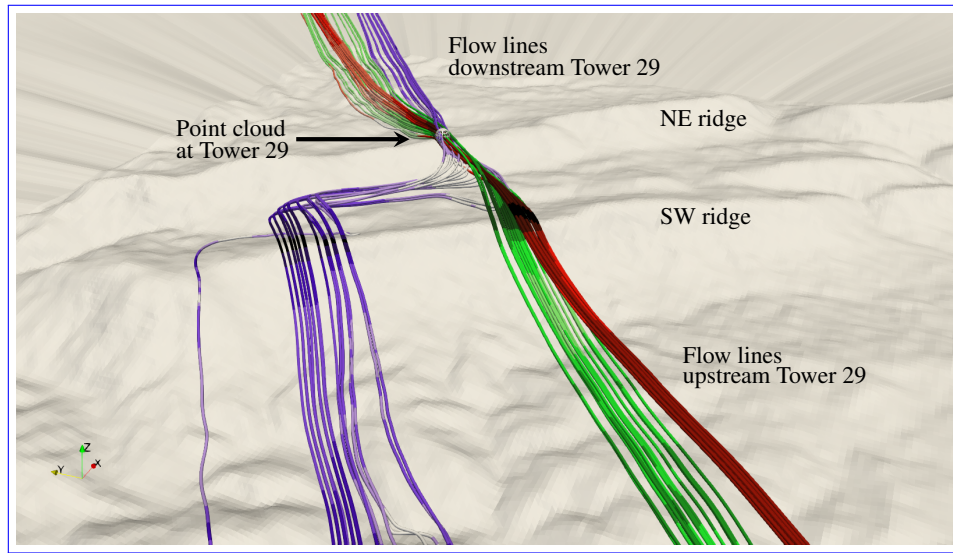
(a) Tower 29.
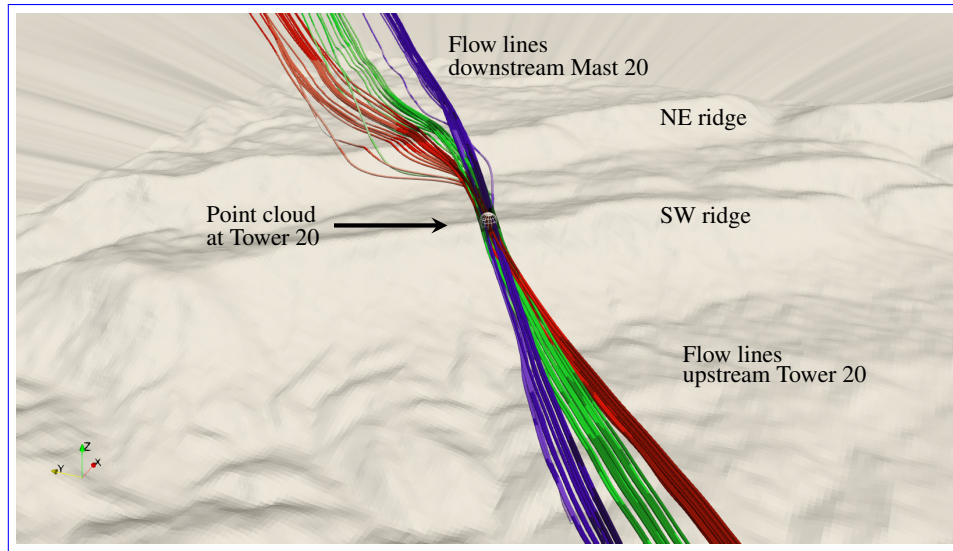
(b) Tower 20.
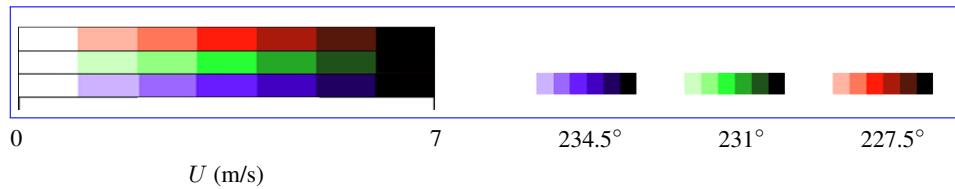
Figure 22. Wind paths of air parcels passing through a sphere of 55 m radius placed on top of the ground at given met mast locations. Flow lines colored in green represent trajectories for wind coming from 231° at the inlet, while red and blue lines illustrate wind at the inlet from 227.5° and 234.5° correspondingly.

5 Conclusions

A Reynolds-averaged Navier-Stokes (RANS) model is set up using OpenFOAM (version 2012) to simulate a 30-minute averaged stationary period corresponding to near-neutral conditions at met-mast Tower 20 located at the Southwest ridge. In that period and for that tower, the wind comes from Southwest at 231° at 100 m height above ground. Five different models are simulated comprising of different source terms to account for the effects of the canopy, the Coriolis force and pressure gradient force, and two different inflow profiles. One idealized set with a log-law velocity profile, and one set of fully developed profiles based on a precursor simulation. Based on the flow topology, the predicted profiles are analyzed in terms of the different groups of towers on top of the ridges and inside the valley. The complex terrain site of Perdigão represents a large spatial variability of forest canopy and surface elevation, which contribute to variable flow topology at different met-masts. The key conclusions for different groups of towers are summarised as follows:

a) **For the towers on the Southwest ridge:** The region at the Southwest ridge is a zone of flow acceleration at the first oncoming ridge downstream of the inlet for wind coming from the Southwest. The inflow profiles are calibrated to closely match the wind speed and direction at Tower 20. Using a canopy model (SF3) decreases the velocities near the surface and is a closer match with field data at Tower 34 and 37. Other models over-predict the velocity profile close to the ground. However, the canopy parameters need to be tuned as the surface heterogeneity is not considered, as the prediction accuracy varies at the different locations along the ridge.

b) **For the towers inside the valley:** The valley is a zone of flow re-circulation and comprises lower velocities and higher variability, which remains challenging for prediction models. Moreover, large uncertainties are seen in the wind velocity, wind direction and turbulent kinetic energy profiles for the field measurements. The prediction capabilities of the models vary with the location of the tower inside the valley. At all towers inside the valley, the SF1 model (k-ϵ) provides the best prediction for wind velocity. Most models show large relative errors in wind speed and turbulent kinetic energy profiles, especially close to the ground.

c) **For the towers on the Northeast ridge**: The region at the Northeast ridge is a zone of flow acceleration downstream of the re-circulation zone from the valley. The canopy model (SF3) provides a strong under-prediction, while all other models provide a prediction within one standard deviation of the field measurements. Predicting the extent of the re-circulation inside the valley and the re-attachment location plays a key role in the prediction profiles on the Northeast ridge. Significant turbulence is seen close to the ground in the field measurements and is under-predicted by most models.

d) **Influence of wind direction:** A significant difference in the wind profiles is seen using different inflow directions. The extent of the re-circulation zone and the re-attachment downstream of the valley is different due to different trajectories taken by the inflow wind profiles coming from the South-West ridge. These uncertainties also depend on the turbulence model and source terms utilized.

Finally, the ~~choice of the~~ best turbulence model ~~is found to be~~ choice is inconclusive in terms of overall prediction capability for different parts of the terrain. In the future, the surface heterogeneity of ~~canopy is to be modelled~~ the canopy could be modeled based on the surface roughness length map at Perdigão. It would be more correct to use different patches with different heights, as seen in the forest point cloud data. Simulations using non-uniform leaf area density could also be performed. ~~An important aspect that needs to be assessed is the effect of inflow wind direction uncertainty on the predictions at different tower locations.~~

Acknowledgements. The authors acknowledge the European Commission for its financial support through the project H2020-MSCA-ITN-2019 zEPHYR (Grant Agreement No. 860101). Perdigao data provided by NCAR/EOL under the sponsorship of the National Science Foundation. https://data.eol.ucar.edu/ The authors would like to thank Paul van der Laan for his useful insights, review, and comments which helped improve the quality of the manuscript.

Author contributions: KV conceived, coordinated and was responsible for both the work, the manuscript writing, and the review process. TOH carried out the numerical simulations, manuscript writing, and preparation of figures, and attended in the review process. SB helped with conception, manuscript writing and review. KEG helped with model setup and review.

Competing interests: The authors declare that they have no conflict of interest.

Data availability: A community has been setup in Zenodo (https://zenodo.org/communities/zephyr/). A repository of the numerical setup shall be added through Github (https://github.com/kartikv95/WESC-Perdigao).

355 References

Alletto, M., Radi, A., Adib, J., Langner, J., Peralta, C., Altmikus, A., and Letzel, M. (2018). E-wind: Steady state cfd approach for stratified flows used for site assessment at enercon. *Journal of Physics: Conference Series*, 1037:072020.

Bechmann, A., Berg, J., Courtney, M., Jørgensen, H., Mann, J., and Sørensen, N. (2009). The bolund experiment: Blind comparison of models for wind in complex terrain (invited). *AGU Fall Meeting Abstracts*.

360 Blackadar, A. K. (1962). The Vertical Distribution of Wind and Turbulent Exchange in a Neutral Atmosphere. *Journal of Geophysical Research*, 67(3):3095.

Blocken, B. (2014). 50 years of computational wind engineering: Past, present and future. *Journal of Wind Engineering and Industrial Aerodynamics*, 129:69–102.

Brower, M. (2012). Findings of investigations into under-performing sites. In *Proceedings of EWEA Technology Workshop, Lyon, France.*
365 European Wind Energy Association (EWEA).

Carvalho, J. P. D. B. (2019). Analysis of stationary periods during the Perdigao 2017 campaign. Master's thesis, University of Porto, Portugal.

Chavez, R., Rodrigo, J., and Gancarski, P. (2014). Modelling of atmospheric boundary-layer flow in complex terrain with different forest parameterizations. volume 524.

Costa, J. C. L. (2007). Atmospheric flow over forested and non-forested complex terrain.

370 Desmond, C., Watson, S., and Hancock, P. (2017). Modelling the wind energy resources in complex terrain and atmospheres. numerical simulation and wind tunnel investigation of non-neutral forest canopy flows. *Journal of Wind Engineering and Industrial Aerodynamics*, 166:48–60.

Emeis, S. (2018). *Wind Energy Meteorology*, volume 2 of *Atmospheric Physics for Wind Power Generation*. Springer International Publishing, Belgium.

375 Fernando, H., Mann, J., Laginha Palma, J., Lundquist, J., Barthelmie, R., Belo-Pereira, M., Brown, W., Chow, F., Gerz, T., Hocut, C., Klein, P., Leo, L., Matos, J., Oncley, S., Pryor, S., Bariteau, L., Bell, T., Bodini, N., Carney, M., and Wang, Y. (2018). The perdigão: Peering into microscale details of mountain winds. *Bulletin of the American Meteorological Society*, 100.

Finnigan, J. (2000). Turbulence in plant canopies. ann rev fluid mech. *Annual Review of Fluid Mechanics*, 32:519–571.

Hågbo, T.-O. and Giljarhus, K. E. T. Pedestrian wind comfort assessment using cfd simulations with varying number of wind directions.
380 *Frontiers in Built Environment*, page 110.

Hågbo, T.-O., Giljarhus, K. E. T., and Hjertager, B. H. (2020). Influence of geometry acquisition method on pedestrian wind simulations. *arXiv preprint arXiv:2010.12371*.

Hargreaves, D. and Wright, N. G. (2007). On the use of the k–ε model in commercial cfd software to model the neutral atmospheric boundary layer. *Journal of wind engineering and industrial aerodynamics*, 95(5):355–369.

385 Jørgensen, H., Nielsen, M., Barthelmie, R., and Mortensen, N. (2005). Modelling offshore wind resources and wind conditions. *In Proceedings (CD-ROM) Copenhagen Offshore Wind.*

Kaimal, J. C. and Finnigan, J. J. (1994). *Atmospheric boundary layer flows: Their structure and measurement*. Oxford University Press.

Koblitz, T. (2013). *CFD Modeling of Non-Neutral Atmospheric Boundary Layer Conditions*. PhD thesis, Denmark.

Laginha Palma, J., Silva, C., Costa Gomes, V., Lopes, A., Esteves, T., and Batista, V. (2020). The digital terrain model in the computational
390 modelling of the flow over the perdigão site: the appropriate grid size. *Wind Energy Science*, 5:1469–1485.

Lalic, B. and Mihailovic, D. (2004). An empirical relation describing leaf-area density inside the forest for environmental modeling. *Journal of Applied Meteorology - J APPL METEOROL*, 43:641–645.

Queck, R., Bienert, A., Maas, H.-G., Harmansa, S., Goldberg, V., and Bernhofer, C. (2012). Wind fields in heterogeneous conifer canopies: Parameterisation of momentum absorption using high-resolution 3d vegetation scans. *European Journal of Forest Research*, 131:165–176.

395 Richards, P. and Hoaxey, R. (1993). Appropriate boundary conditions for computational wind engineering models using the k-ϵ turbulence model. In Murakami, S., editor, *Computational Wind Engineering 1*, pages 145–153. Elsevier, Oxford.

Rodrigo, J., Santos, P., Chavez, R., Avila, M., Cavar, D., Lehmkuhl, O., Owen, H., Li, R., and Tromeur, E. (2021). The alex17 diurnal cycles in complex terrain benchmark. *Journal of Physics: Conference Series*, 1934:012002.

Salmon, J., Bowen, A., Hoff, A., Johnson, R., Mickle, R., Taylor, P., Tetzlaff, G., and Walmsley, J. (1988). The askervein hill project: Mean
400 wind variations at fixed heights above ground. *Boundary-Layer Meteorology*, 43:247–271.

Schmidt, J., Peralta, C., and Stoevesandt, B. (2012). Automated generation of structured meshes for wind energy applications. Open Source CFD International Conference, London.

Sogachev, A. (2009). A note on two-equation closure modelling of canopy flow. *Boundary-Layer Meteorology*, 130:423–435.

Sogachev, A. and Panfyorov, O. (2006). Modification of two-equation models to account for plant drag. *Boundary-Layer Meteorology*,
405 121:229–266.

Sørensen, N. N., Bechmann, A., Réthoré, P.-E., Cavar, D., Kelly, M. C., and Troen, I. (2012). How fine is fine enough when doing CFD terrain simulations. In *EWEA 2012-European Wind Energy Conference & Exhibition*, pages 1167–1172. European Wind Energy Association (EWEA).

Temel, O., Bricteux, L., and Beeck, J. (2018). Coupled wrf-openfoam study of wind flow over complex terrain. *Journal of Wind Engineering*
410 *and Industrial Aerodynamics*, 174:152–169.

van der Laan, M. P., Baungaard, M., and Kelly, M. (2021a). Inflow modeling for wind farm flows in rans. *Journal of Physics: Conference Series*, 1934:012012.

van der Laan, M. P., Kelly, M., and Baungaard, M. (2021b). A pressure-driven atmospheric boundary layer model satisfying rossby and reynolds number similarity. *Wind Energy Science*, 6:777–790.

415 van der Laan, M. P., Kelly, M., Floors, R., and Peña, A. (2020). Rossby number similarity of an atmospheric rans model using limited-length-scale turbulence closures extended to unstable stratification. *Wind Energy Science*, 5:355–374.

Vasiljevic, N., Laginha Palma, J., Angelou, N., Matos, J., Menke, R., Lea, G., Mann, J., Courtney, M., Frölén Ribeiro, L., and Costa Gomes, V. (2017). Perdigão 2015: methodology for atmospheric multi-doppler lidar experiments. *Atmospheric Measurement Techniques Discussions*, pages 1–28.

420 Vassallo, D., Krishnamurthy, R., Menke, R., and Fernando, H. (2020). Observations of stably stratified flow through a microscale gap. *Journal of the Atmospheric Sciences*, 78.

Wagner, J., Wildmann, N., and Gerz, T. (2019). Improving boundary layer flow simulations over complex terrain by applying a forest parameterization in WRF. *Wind Energ. Sci. Discuss. [preprint]*.

Yang, Y., Gu, M., Chen, S., and Jin, X. (2009). New inflow boundary conditions for modelling the neutral equilibrium atmospheric boundary
425 layer in computational wind engineering. *Journal of Wind Engineering and Industrial Aerodynamics*, 97(2):88–95.

Appendix

Grid Independence ~~study~~Study

~~A mesh refinement study has been performed as shown in Table 7, by increasing the number of cells in the x and y direction thereby increasing the horizontal mesh resolution. The case has been simulated using the standard~~ The structured grids are
430 generated using the `terrainBlockMesher` tool (Schmidt et al., 2012), which interpolates the SRTM terrain data and creates the terrain patch, which is blended into a cylindrical domain. The simulation inflow profiles for all the meshes are calibrated to match the field experiment at 100 m of Tower 20 (tse04) on the South-West ridge. A convergence of the wind profiles is seen at towers across the towers on the South-West ridge, inside the valley and on the North East ridge. The simpleFoam (SF1) solver with the $k - \epsilon$ turbulence model ~~with an idealized set of inlet profiles including a~~
435 ~~logarithmic velocity profile, and no Coriolis or pressure gradient source term.~~ setup is utilized for the study. The medium case is chosen for the present mesh study The mesh resolution cases are well within the recommendations provided by Palma *et al.* (Laginha Palma et al., 2020).

Table 7. Grid refinement study parameters showing the number of cells per main direction.

Case	Nx	Ny	Nz	NCells (million)
Coarse	~~227~~550	~~227~~550	~~120~~150	~~12.7~~62
Medium	~~332~~600	~~332~~600	~~120~~170	~~21.19~~88
Fine	~~469~~650	~~469~~650	~~120~~190	~~30.6~~115

~~Negligible differences are seen in the velocity and turbulent kinetic energy profiles on top of the ridge at the Tower 20 (Calibration tower) on the South West ridge seen in Fig ?? and at Tower 29 close to 100 m on the North East ridge seen in~~
440 ~~Fig ??. However, larger differences are seen close to the ground as the topology of terrain is further resolved near the surface upon grid refinement. The structured grids are generated using the `terrainBlockMesher` tool (Schmidt et al., 2012), which interpolates the SRTM terrain data and creates the terrain patch which on which smoothing is applied towards a cylindrical domain on the sides. Increasing the number of cells refines and slightly modifies the surface mesh close to the ground. Similar differences are seen when using different terrain databases in the grid refinement study by (Laginha Palma et al., 2020)~~
445 ~~. Furthermore, a small change in the prediction of extent of the re-circulation zone could have a significant change and uncertainty in the predictions inside the valley in Fig. ?? on top of the Northeast ridge.~~

Inflow profiles - precursor and log-law

~~Two~~ As shown in Fig 26, two sets of inflow profiles are utilized~~as shown in Fig 26~~. An idealized set of inlet profiles, including a logarithmic velocity profile, and a fully developed profile using a precursor driven by a Coriolis force and a pressure gradient
450 force. The inflow velocity profiles are calibrated to reach the desired inflow conditions at the met-mast Tower 20 at a height 100 m, for a time period identified as neutral based on the Bulk Richardson number. The wind velocity magnitude profiles ~~is~~
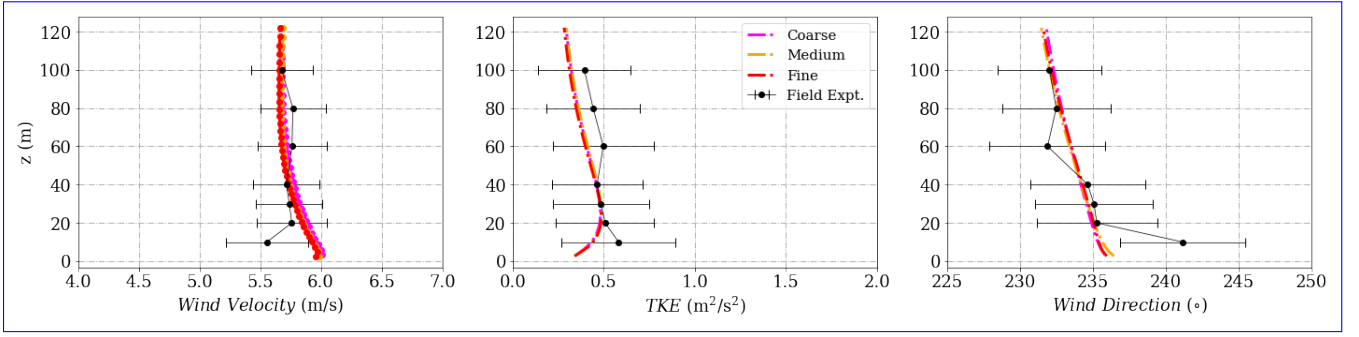
Figure 23. ~~Profiles for~~ a) ~~Velocity~~ Wind velocity magnitude b) Wind direction c) Turbulent kinetic energy ~~c) Meteorological wind direction~~ tuned to reach calibration at height 573 m corresponding to 100 m at Tower 20 (tse04)~~on the Southwest ridge, shown for different levels of grid refinement.~~
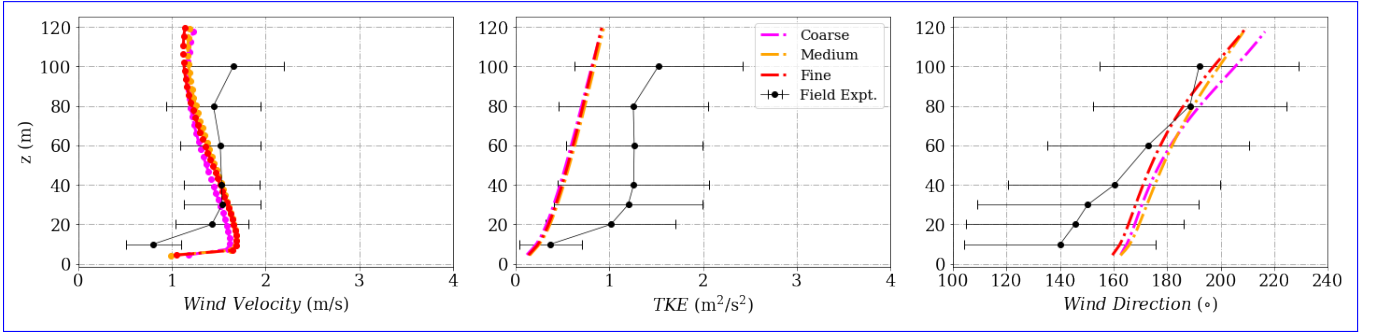
Figure 24. ~~Profiles for~~ a) ~~Velocity~~ Wind velocity magnitude b) Wind direction c) Turbulent kinetic energy ~~c) Meteorological wind direction~~ at Tower ~~29~~ 25 (~~tse13~~tse09)~~on the Northeast ridge, shown for different levels of grid refinement~~
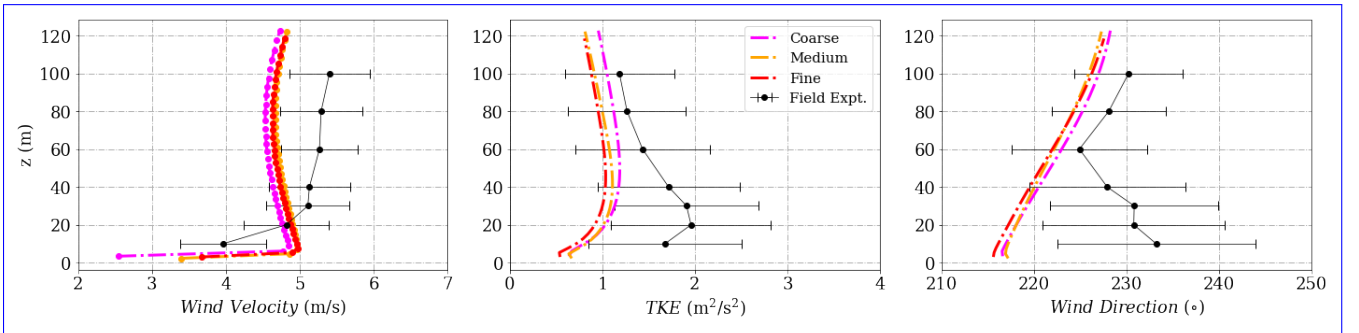
Figure 25. ~~Profiles for~~ a) ~~Velocity~~ Wind velocity magnitude b) Wind direction c) Turbulent kinetic energy ~~c) Meteorological wind direction~~ at Tower ~~25~~ 29 (~~tse09~~tse13)~~inside the valley, shown for different levels of grid refinement~~
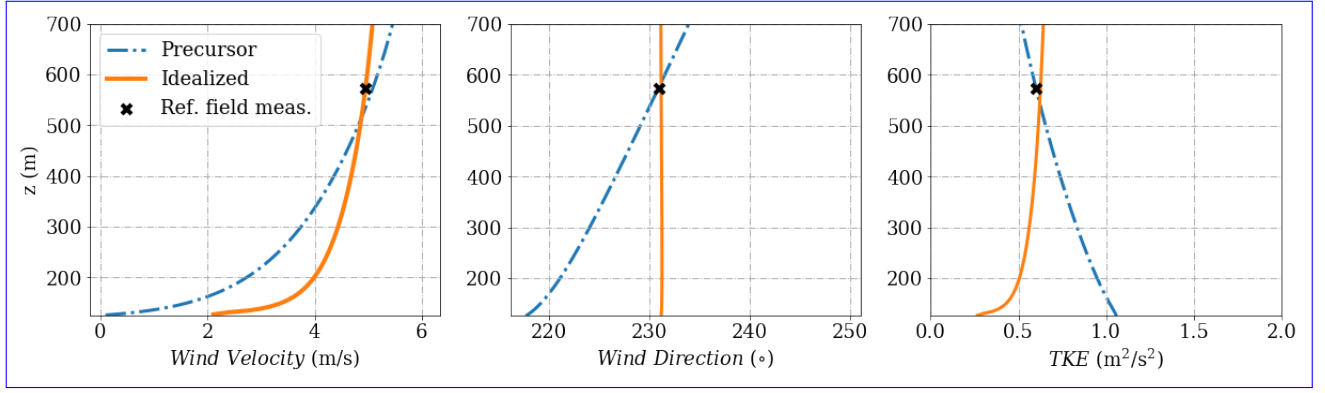
Figure 26. Idealized and Precursor (developed) input profiles for a) Wind velocity magnitude b) Wind direction c) Turbulent kinetic energy tuned to reach calibration at height 573 m corresponding to 100 m at Tower 20 (tse04)

are close to logarithmic. For the wind direction, the idealized profile fixes a uniform wind direction, but the precursor has a source term to account for the Coriolis effect, so a wind veer is seen over the entire height. Finally, for the TKE, a profile is set in the idealized case while for the precursor developed profile it is limited by the maximum mixing length scale~~, hence there~~

455   ~~is a decrease in turbulence levels over height~~. Increasing the roughness length z0 of the precursor to 6 (m), while also tuning pressure gradient magnitude and direction to get the right wind speed, wind direction, and now TKE at the reference height to match the meet the average field experiment value at the calibration point.

Governing equations

The equations solved for the buoyantBoussinesqSimpleFoam solver are the continuity equation (Eqn. 3), momentum equa-

460   tion (Eqn. 4) and turbulence transport (Eqn. 6, 7), temperature (Eqn. 5) as described by Alletto et al. (2018). The pressure gradient (π_i) drives the momentum equation ~~,~~ and the source terms for Coriolis and canopy effects are included in the momentum equation. The buoyancy terms are only added in the turbulence transport equations, but are set to zero for the present neutral case. The equation for turbulent dissipation rate contains the maximum length turbulence scale limiter (l_{max}) to modify the mixing-length scale estimations for setting different atmospheric stabilities. This description has been added to the

465   Appendix of the manuscript.

$$\frac{\partial \rho \bar{u}_i}{\partial x_i} = 0 \tag{3}$$

$$\frac{\partial \rho \bar{u}_i}{\partial t} + \frac{\partial \rho \bar{u}_i \bar{u}_j}{\partial x_j} - \frac{\partial}{\partial x_j}\left(\rho(v+v_t)\left(\frac{\partial \bar{u}_i}{\partial x_j} + \frac{\partial \bar{u}_j}{\partial x_i}\right)\right) = -\frac{\partial \bar{p}}{\partial x_i} - \pi_i - \rho\epsilon_{ijk}f_j\bar{u}_k - \rho c_d \Sigma \bar{u}_i |\bar{u}| \tag{4}$$

$$\frac{\partial \rho \bar{\theta}}{\partial t} + \frac{\partial \rho \bar{u}_i \bar{\theta}}{\partial x_i} - \frac{\partial}{\partial x_i}\left(\rho\left(v + \frac{v_t}{\sigma_\theta}\right)\frac{\partial \bar{\theta}}{\partial x_i}\right) = S_\theta \tag{5}$$

$$\frac{\partial k}{\partial t} + \bar{u}_j \frac{\partial k}{\partial x_j} - \frac{\partial}{\partial x_j}\left(\left(v + \frac{v_t}{\sigma_k}\right)\frac{\partial k}{\partial x_j}\right) = P_k - \varepsilon + B \tag{6}$$

$$\frac{\partial \varepsilon}{\partial t} + \bar{u}_j \frac{\partial \varepsilon}{\partial x_j} - \frac{\partial}{\partial x_j}\left(\left(v + \frac{v_t}{\sigma_\varepsilon}\right)\frac{\partial \varepsilon}{\partial x_j}\right) = \left(C_{\varepsilon1} + (C_{\varepsilon2} - C_{\varepsilon1})\left(\frac{l}{l_{\max}}\right)^a\right)\frac{\varepsilon}{k}P - C_{\varepsilon2}\frac{\varepsilon^2}{k} +$$
$$((C_{\varepsilon1} - C_{\varepsilon2})\alpha_B)\frac{\varepsilon}{k}B - (C_{\varepsilon1} - C_{\varepsilon2})\frac{\varepsilon}{k}S_d \tag{7}$$

470

Influence of Wind Direction using other models

SF2 $k - \omega$

The influence of wind direction change using the SF2 ($k - \omega$) model at different towers is shown in Figs 27, 28 and 29 respectively. The results appear to be similar to the SF1 ($k - \epsilon$) model. However in comparison a lesser difference is seen in
475 the profiles between the $231°$ and the $234.5°$ degree cases at Towers 25 and 29.
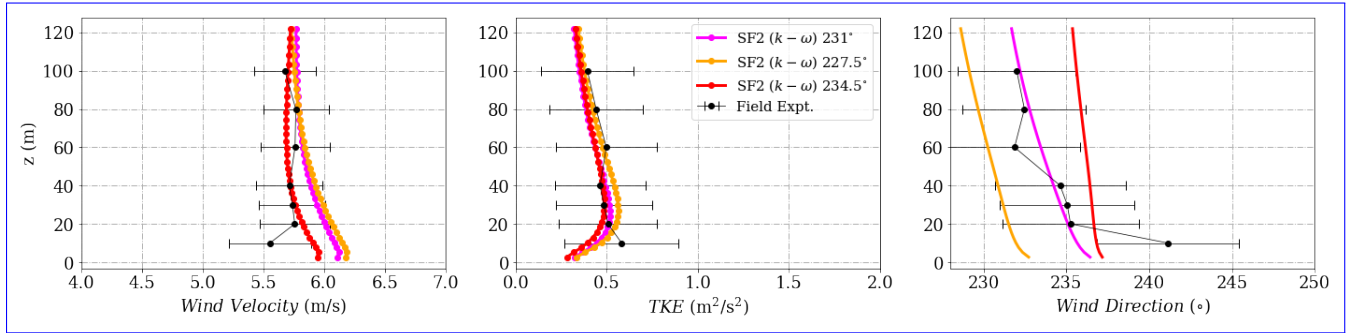
Figure 27. a) Wind velocity magnitude b) Wind direction c) Turbulent kinetic energy tuned to reach calibration at height 573 m corresponding to 100 m at Tower 20 (tse04) for the SF2 ($k - \omega$) model.

SF3 Canopy

The influence of wind direction change using the SF3 (Canopy) model at different towers is shown in Figs 30, 31 and 32 respectively. A much larger difference in wind profiles is seen at Tower 29 on the North-East ridge compared to the SF1 ($k - \epsilon$) model indicating larger uncertainties with wind direction. Presently, the canopy is modeled using a uniform tree height, and
480 perhaps there would be higher uncertainties with a non-uniform canopy across the domain, the path taken by the wind for different inflows would vary significantly. A much different re-circulation zone is developed, as seen in the wind direction profiles.
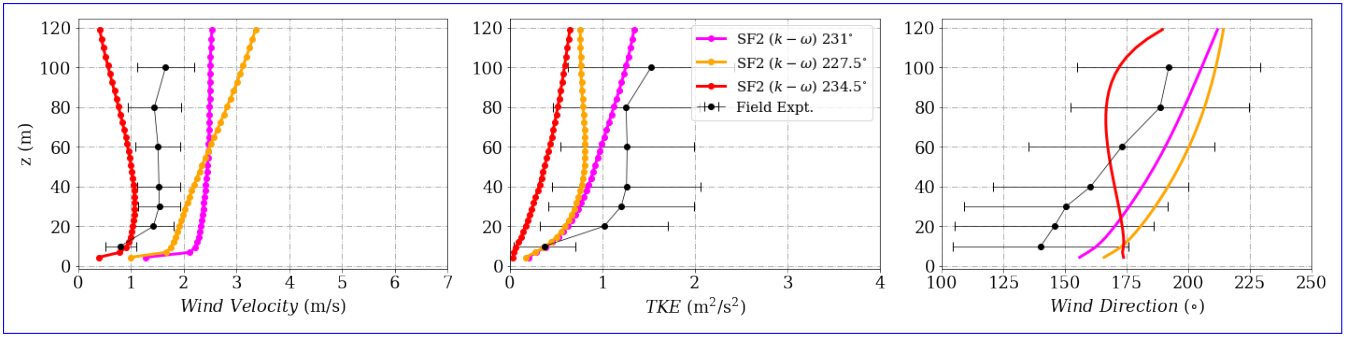
Figure 28. a) Wind velocity magnitude b) Wind direction c) Turbulent kinetic energy at Tower 25 (tse09) for the SF2 $(k - \omega)$ model.
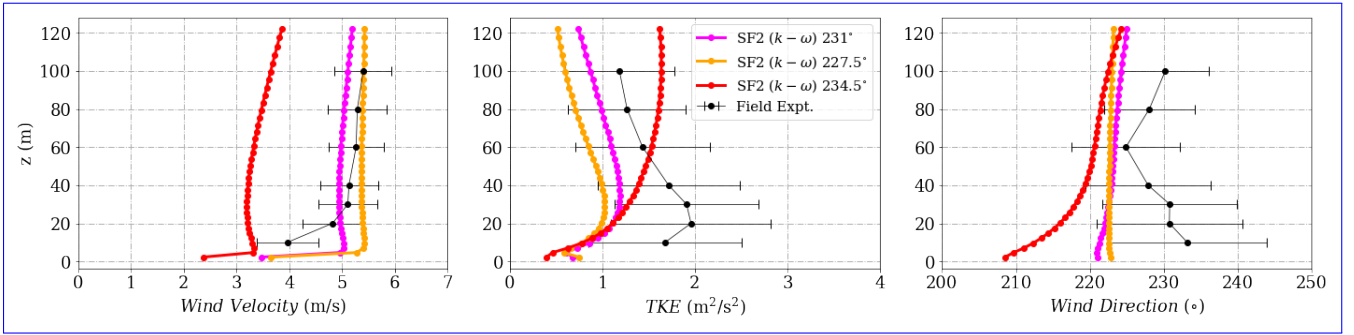
Figure 29. a) Wind velocity magnitude b) Wind direction c) Turbulent kinetic energy at Tower 29 (tse13) for the SF2 $(k - \omega)$ model.
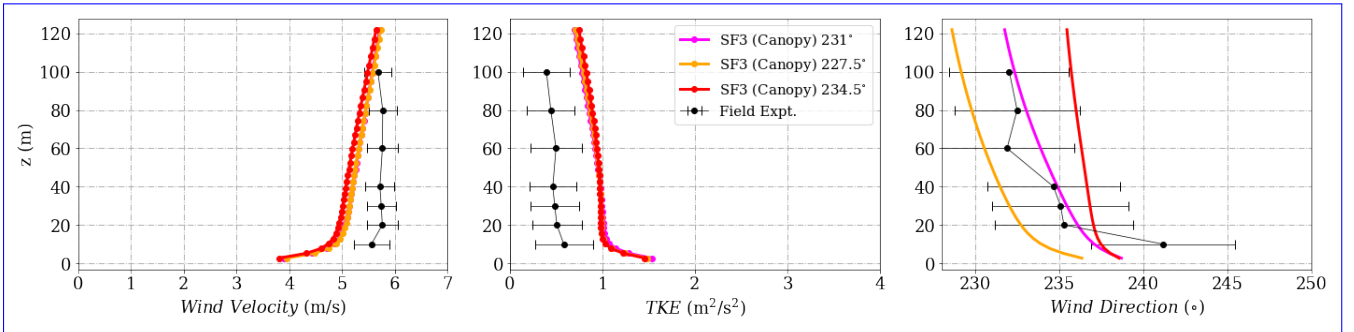
Figure 30. a) Wind velocity magnitude b) Wind direction c) Turbulent kinetic energy tuned to reach calibration at height 573 m corresponding to 100 m at Tower 20 (tse04) for the SF3 (Canopy) model.
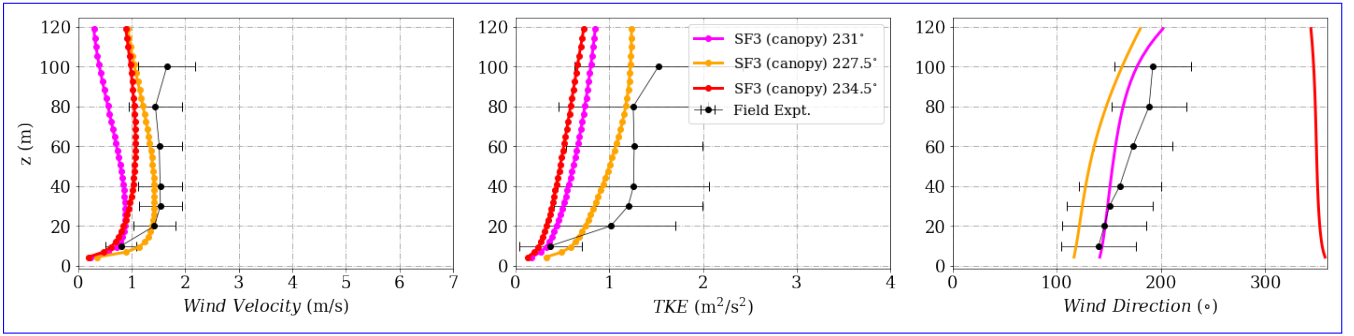
Figure 31. a) Wind velocity magnitude b) Wind direction c) Turbulent kinetic energy at Tower 25 (tse09) for the SF3 (Canopy) model.
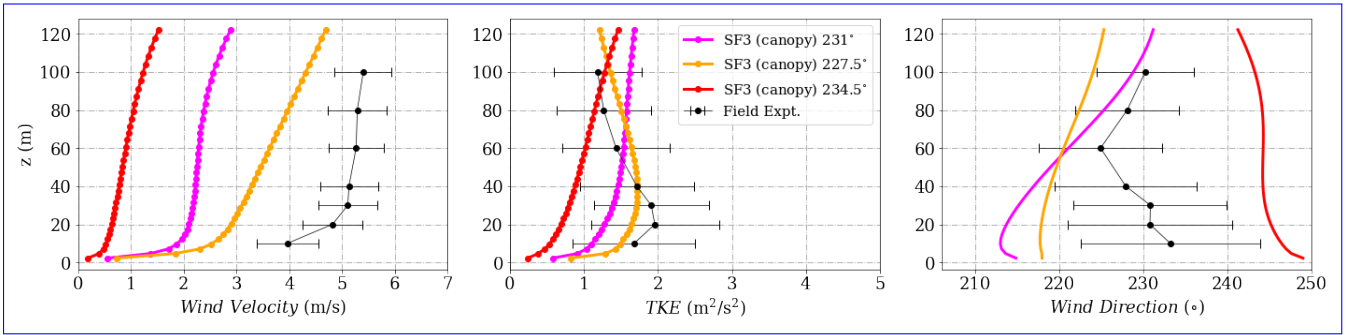
Figure 32. a) Wind velocity magnitude b) Wind direction c) Turbulent kinetic energy at Tower 29 (tse13) for the SF3 (Canopy) model.

SF4 Coriolis

The influence of wind direction change using the SF3 (Coriolis) source term model at different towers is shown in Figs 33, 34 and 35 respectively. Interestingly, for this case, the flow difference between the $231°$ and the $234.5°$ degree cases at Towers 25 and 29 is relatively small compared to the SF1 $k - \epsilon$ case. With the Coriolis source term, the flow turning due to the Coriolis effect is accounted for, and hence the inflow wind for calibration is set accordingly to obtain the required wind direction at the calibration mast. Consequently, the path taken by the wind across the terrain is different.

BBSF

Figs 36,37 and 38 show the wind profiles for the BBSF simulation model with the precursor inflow. Here the inflow from wind direction $234.5°$ shows a larger difference between the bother profiles even at the calibration mast, and a decrease in wind velocity at Tower 29 on the North-East Ridge, similar to the other models. The wind direction standard deviation bounds in Fig 38 appear to be more closely predicted by this model.
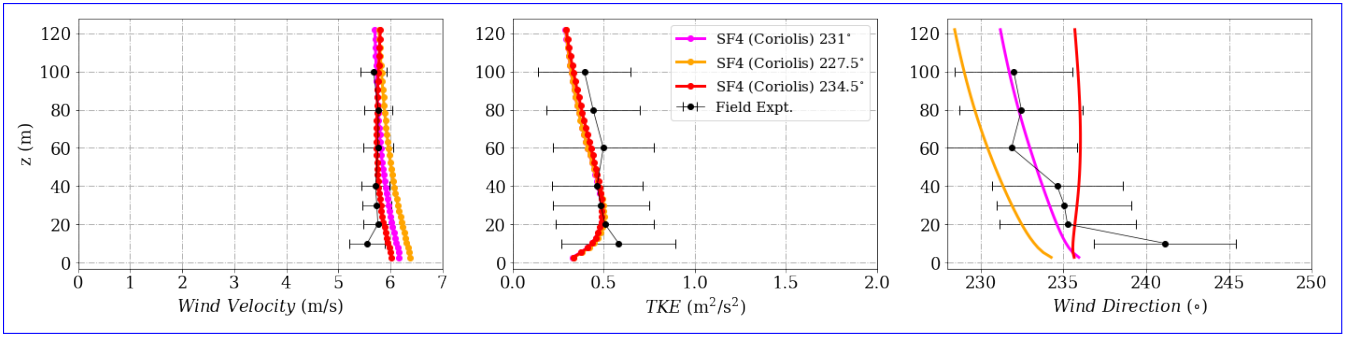
Figure 33. a) Wind velocity magnitude b) Wind direction c) Turbulent kinetic energy tuned to reach calibration at height 573 m corresponding to 100 m at Tower 20 (tse04) for the SF4 (Coriolis) model.
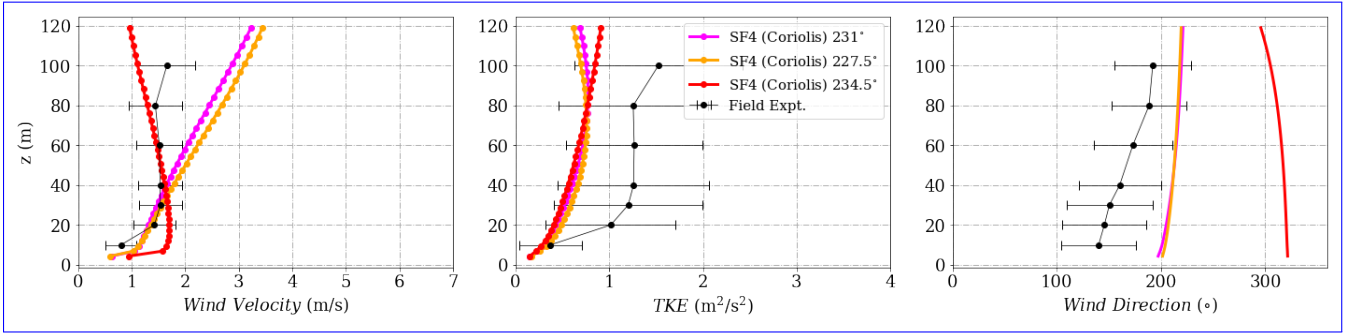
Figure 34. a) Wind velocity magnitude b) Wind direction c) Turbulent kinetic energy at Tower 25 (tse09) for the SF4 (Coriolis) model.
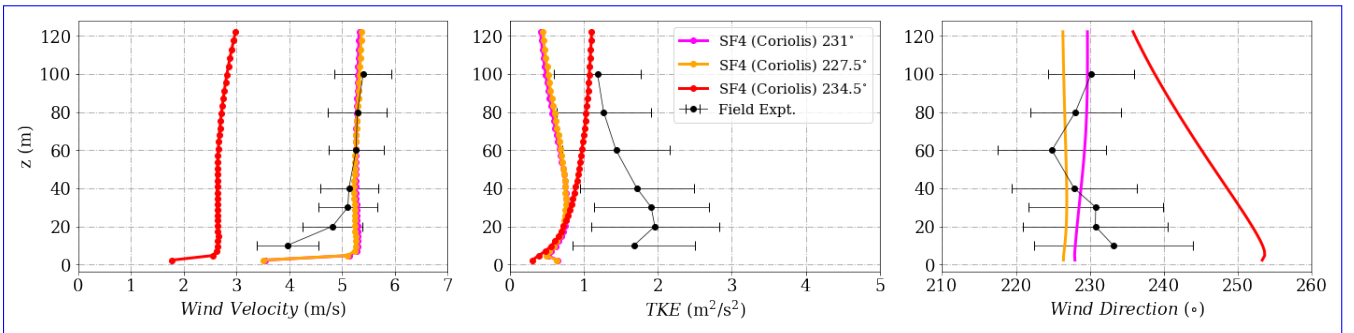
Figure 35. a) Wind velocity magnitude b) Wind direction c) Turbulent kinetic energy at Tower 29 (tse13) for the SF4 (Coriolis) model.
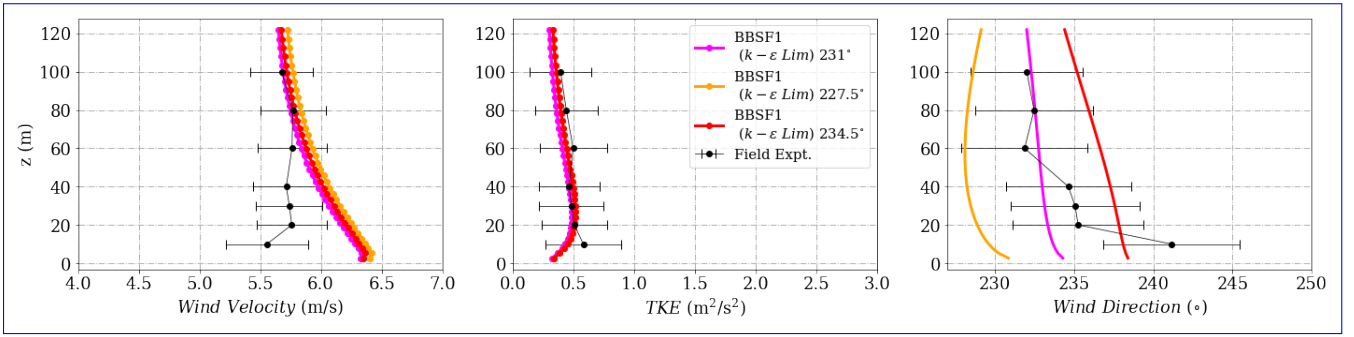
Figure 36. a) Wind velocity magnitude b) Wind direction c) Turbulent kinetic energy tuned to reach calibration at height 573 m corresponding to 100 m at Tower 20 (tse04) for the BBSF model.
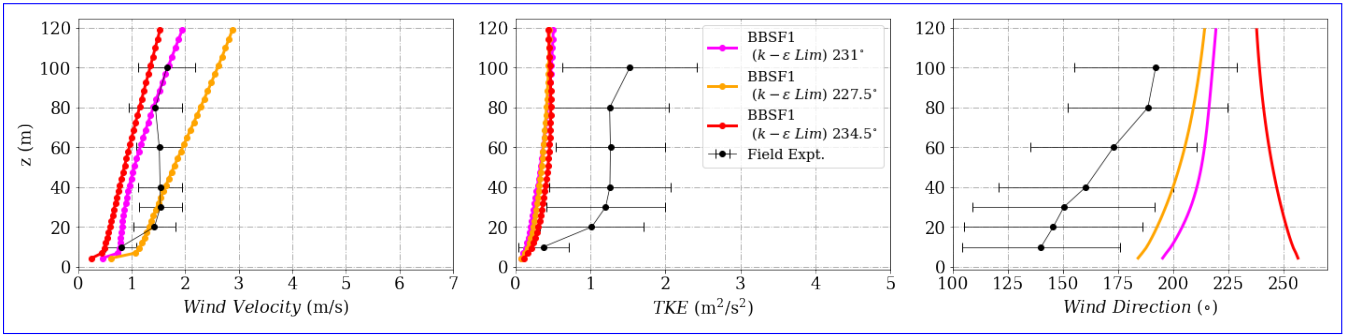
Figure 37. a) Wind velocity magnitude b) Wind direction c) Turbulent kinetic energy at Tower 25 (tse09 for the BBSF model.
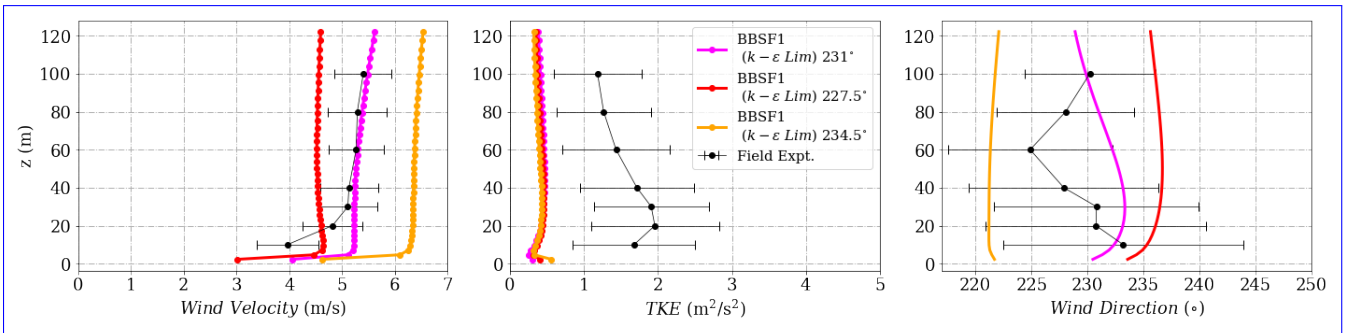
Figure 38. a) Wind velocity magnitude b) Wind direction c) Turbulent kinetic energy at Tower 29 (tse13) for the BBSF model.